Solid Earth Discuss., doi:10.5194/se-2017-30, 2017
Manuscript under review for journal Solid Earth
Discussion started: 20 March 2017

Solid Earth
Discussions
Open Access
EGU

The grain size(s) of Black Hills Quartzite deformed in the dislocation creep regime.

Renée Heilbronner[1),2)] and Rüdiger Kilian[1)]

[1)] Geological Institute, Basel University, Bernoullistrasse 32, CH_4056 Basel, Switzerland

[2)] Institutt for geovitenskap, UiT Norges arktiske universitet, Dramsveien 201, N-9037 Tromsø, Norway

Dedication

This contribution is dedicated to Jan Tullis whose superb work on experimental rock deformation and microstructure analysis continues to be an inspiration to us all.

Abstract

A number of general shear experiments on Black Hills Quartzite (BHQ) in the dislocation creep regime, 5 of which have been analyzed previously using the CIP method (Heilbronner & Tullis, 2002 and 2006), are (re-)examined using the higher spatial and orientational resolution of EBSD. Segmentations based on c-axis orientation and on full crystallographic orientations are compared. Texture domains of preferred c-axis orientation are extracted and analyzed separately. Subdomains are recognized and their shape and size is related the kinematic framework and the original grains in the BHQ. Grain size analysis using a segmentation based on c-axis orientations is carried out for all, high and low strain samples of all regimes, and for a number of texture domains. The results are compared to the recrystallized quartz piezometer of Stipp & Tullis (2003), returning consistently higher values for stress or grain size. Possible causes for the discrepancy are texture dependence, grain scale strain, and dependence on the kinematic framework (in axial versus general shear experiments).

Solid Earth Discuss., doi:10.5194/se-2017-30, 2017
Manuscript under review for journal Solid Earth
Discussion started: 20 March 2017

Keywords:
Recrystallized grain size, quartz piezometer, CIP-EBSD comparison, grain boundary detection, texture domains

1. Introduction

Black Hills Quartzite (BHQ) has been used extensively in experimental rock deformation for numerous studies. Coaxial and general shear experiments have been carried out, for example, to define the dislocation creep regimes of quartz (Hirth & Tullis, 1992), to derive flow law parameters (Gleason & Tullis ,1995), to determine the effect of annealing (Heilbronner & Tullis, 2002; Kidder et al., 2016), effect of the chemical environment on deformation processes (Post et al, 1996; Chernak et al., 2009), to compare deformation processes to nature (Stipp & Kunze, 2008) or to study the development of texture and microstructure with strain (Tullis et al., 1973; Tullis, 1977; Dell'Angelo & Tullis, 1989; Gleason et al., 1993; Heilbronner & Tullis, 2006). BHQ was also used to determine the widely used recrystallized quartz grain size piezometer of Stipp & Tullis (2003) (Stipp et al., 2006).

Among the microstructure analyses that were performed in those original papers, grain size was usually determined using CIP misorientation images. However, the CIP method (= computer-integrated polarization microscopy, details in Heilbronner and Barrett, 2014) is only capable of detecting the c-axis orientation of optically uniaxial materials and hence is only capable of detecting grain boundaries between grains that differ in c-axis orientation.

One of the puzzling results found by Heilbronner & Tullis (2006) was that the recrystallized grain size seemed to depend on the crystallographic preferred orientation of the grains within a domain. In other words the grain size seemed to not only depend on the flow stress but also on the orientation of the c-axis with respect to the kinematic framework. At the time, no EBSD analysis (electron back scatter diffraction) was carried out and hence the full crystallographic orientation was not known. In principle it is therefore possible that some grain boundaries were missed (between grains with parallel c-axes) and the grain sizes miscalculated.

Orientation tracking and ACF (autocorrelation function) shape analysis of the so-called 'prism' domains (with c-axes approximately parallel to the structural Y

Solid Earth Discuss., doi:10.5194/se-2017-30, 2017
Manuscript under review for journal Solid Earth
Discussion started: 20 March 2017

direction) showed that these domains grow or as a function of strain beyond the size of the original BHQ grain size, forming lenticular aggregates that are more elongated and less rotated than the other domains. Together with the extra large grain size, this suggested that they deform at lower stresses than the other domains.

In a set of shear experiments on quartz gouge at the brittle-viscous transition (Richter et al., 2016), flow stresses could be calibrated very accurately and EBSD was used to measure the recrystallized grain size. In order to compare the recrystallized grain size of crushed quartz crystals to that of solid quartzite (BHQ), the samples of the 2006 experiments (deformed in the dislocation creep regimes 1, 2 and 3) are re-measured, using EBSD data sets to determine the grain size, but also, more generally, to repeat, refine and expand the microstructure and texture analysis of Heilbronner & Tullis (2006). In this study the focus is on the recrystallized grain size with the aim (a) of comparing CIP- and EBSD derived grain size measurements, (b) of confirming or rejecting the notion that the recrystallized grain size depends on texture, and (c) of checking if the stress dependence of the recrystallized grain size falls on the quartz piezometer of Stipp and Tullis (2003).

Solid Earth Discuss., doi:10.5194/se-2017-30, 2017
Manuscript under review for journal Solid Earth
Discussion started: 20 March 2017

2. Selected deformation experiments

2.1. Deformation experiments

The rock deformation experiments that produced the samples analyzed in this study are described in Heilbronner & Tullis (2006). A solid medium confining pressure apparatus is used, and approximately 1.25 mm thick slices of Black Hills quartzite (BHQ) were placed at an angle of 45° between forcing blocks as shown in Figure 1a. The experiments were run with a confining pressure of approximately 1.5 GPa, and an average shear strain rate of approximately $2 \cdot 10^{-5}$ s^{-1} (see Table 1 for details of experimental conditions). Temperatures were 850°C, 875°C, and 915°C, for regime 1, 2, and 3 respectively, and 0.17 wt% H_2O was added for one of the regime 2 and all of the regime 3 samples. For each regime, one sample was deformed to a relatively low finite shear strain ($2.7 < \gamma < 4.3$) and one or two to a relatively high finite shear strain ($5.8 < \gamma < 7.2$). Note, that shear strain usually reported in the experiments refers to an apparent shear strain, which is calculated as simple shear with respect to the final thickness (thf) of the sample ($\gamma = d/thf$) disregarding the pure shear component associated with the thinning of the sample. This apparent shear strain is numerically larger than the true shear strain, which is not easy to calculate for a thinning shear zone. To correct for the flattening, often the effective shear strain ($\gamma_{effective} = (d/th0)^{(th0/thf)}$) is used, assuming homogeneous general shear (see Table 1)

For this study, the force-displacement records are converted to stress strain curves using a modified version of the rigS program (Richter et al., 2016), taking into consideration the decreasing overlap of the forcing blocks (ACF correction) and the increasing confining pressure resulting from the compression of the confining medium inside the vessel (32 - 33 MPa per mm piston advance depending on temperature). The friction correction (as described in Pec et al. 2015) and the stress correction as proposed by Holyoke & Kronenberg (2010) are omitted. Thinning of the sample is assumed to be linear with the axial advancement of the forcing block (see Figure 2, Pec et al., 2016). For every time step, the shear strain is calculated as the total displacement of the forcing block, at time t, along the shear zone divided by the instantaneous thickness of the shear zone, at time t. The resulting stress strain curves reproduce the curves that were originally published (Figure 1b). This is not surprising

Solid Earth Discuss., doi:10.5194/se-2017-30, 2017
Manuscript under review for journal Solid Earth
Discussion started: 20 March 2017

because (a) the shear strain is calculated in exactly the same way and (b) the effect of the confining pressure correction ('salt correction') is to 'weaken' the sample and thus 'replaces' the effect of the original viscosity correction.

2.2. EBSD data acquisition

Of each of the deformed samples, a polished thin section of approximately 20 µm thickness had been prepared, suitable for the analysis by computer-integrated polarization microscopy (CIP), which was carried out in the previous studies (Heilbronner & Tullis, 2002 and 2006). (The CIP method was introduced by Panozzo Heilbronner & Pauli, 1993, and is described in detail in Heilbronner & Barrett, 2014). The sections are then polished using a Struers Tegramin-30® equipment (3 min, 10 N), with their MD Chem® neopren pad and OP-U® polishing liquid.

EBSD data acquisitian is carried out using a ZEISS Merlin VP Compact® (ZEISS SmartSEM® operating software), a Nordlys Nano Camera operated with Oxford AZtec® software. Using the settings listed in Table 2, maps are acquired at 1, 0.5 and 0.25 µm step size. The data files are exported and the open source MTEX Toolbox (Hielscher & Schaeben, 2008; https://mtex-toolbox.github.io/) is used for further processing and analysis. If necessary, maps are rotated to have the forcing block in a horizontal direction and flipped such that the shear sense is sinistral for all maps, an example is shown in Figure 2a. In order to enable high resolution CIP analysis of the EBSD input, c-axis azimuth and inclination maps are calculated and exported as TIFF images (Figure 2b). Further texture analysis and segmentation is carried out along two lines: (1) using MTEX and the full texture information (2) using CIP (including ImageSXM and/or ImageJ), making use only of the c-axis texture. Note, however, that the input data for both comes from EBSD maps. Details of methods and the results of the EBSD analysis are described in Kilian & Heilbronner (this volume), while the mostly c-axis based CIP analyses are presented in the following.

Solid Earth Discuss., doi:10.5194/se-2017-30, 2017
Manuscript under review for journal Solid Earth
Discussion started: 20 March 2017

3. Image analysis

Image processing, pre-processing and analysis, is carried out using ImageSXM (http://www.liv.ac.uk/~sdb/ImageSXM/), as described in Heilbronner & Barrett (2014). Alternatively, and complementary to Image SXM, the open source software, ImageJ (http://rsb.info.nih.gov/ij) distributed over the Fiji platform (http:// fiji.sc/Fiji) is used.

3.1. Pre-processing

The main task during pre-processing is to remove noise. Two types of noise and their sources need to be distinguished. One is salt-and-pepper noise that shows up as individual pixels with values outside the range of value of its neighbours, the second is statistical noise resulting from the imaging and indexing processes. Examples of the first type are non-indexed or misindexed pixels, the second kind is caused by fluctuations of orientation measurements typically with misorientation angles < 1° for conventional EBSD. Using ImageSXM, the c-axis azimuth (AZI) and the c-axis inclination (INC) image are saved into the red and the green channel of an RGB image, the blue channel is filled with the bitmap of the non-indexed pixels (MASK). Together the image appears in red-yellow-green colours as shown in Figure 23.1 of Heilbronner & Barrett (2014). In one case, 1a-w940, the image is cropped to a region with acceptable indexing (see Table 2 and 3). Misindexed pixels are removed by a process called 'Remove Outliers' (ImageJ) which is applied once for bright and once for dark outliers (using a threshold of 1 and a radius of 1 in both cases). By this process, misindexed and non-indexed pixels are replaced by (AZI / INC) values calculated from the (AZI / INC) values of the neighbouring pixels. After this type of noise cleaning, the percentage of pixels with a valid c-axis directions is considerably increased from an average of 83% to 92% (see Table 3).

The filtered RGB image are separated again, the three individual channels now representing the input images for the CIP software (http:// earth.unibas.ch/micro). For every EBSD map, c-axis orientation images (COI), orientation gradient images (OGI) and misorientation images (MOI) are calculated, as shown in Figure 2b. The COIs can be viewed with different color-look-up tables (CLUT) depending on the desired

Solid Earth Discuss., doi:10.5194/se-2017-30, 2017
Manuscript under review for journal Solid Earth
Discussion started: 20 March 2017

feature to be visualized. Using the Spectrum CLUT allows an easy comparison with published COIs obtained by light-optical methods. A so-called AZI CLUT is used to highlight changes of azimuth irrespective of inclination (see section on subdomains). Note that in the context of CIP, the term 'orientation' refers to 'c-axis orientation', (a 'direction' in terms of full texture), and 'misorientation' refers to the angle between a given c-axis and a reference direction (see Heilbronner & Barret, 2014, chap.23). MOIs show the angle between the c-axis orientations at each pixel and an internal (defined on pole figure) or external (i.e., structural) reference direction, OGIs show the average angular difference of the c-axis orientation of each pixel with respect to those of its (4 or 8) neighbours (Figure 2b). Note, the maximum value for an angle between two c-axes is 90°.

3.2. Segmentation

In order to check if grain boundary maps derived on the basis of the full texture are identical to those obtained through image analysis of c-axis misorientation images (as used for the grain size analyses published by Heilbronner & Tullis, 2002, 2006), two segmentations are performed for every sample, one using the full crystallographic orientation of each pixel, a so-called EBSD segmentation producing EBSD boundaries, and one using c-axis azimuth and inclination images a so-called CIP segmentation producing CIP boundaries, with both types using EBSD mappings as input. An example of such a comparative segmentation is shown in Figure 3. Both methods are some form of image analysis, the EBSD approach proceeding analogous to region growing algorithms, the CIP approach using edge detection and structural filtering.

3.2.1. Procedure to obtain EBSD boundaries:

Segmentation of grains from EBSD data can be accomplished based on a misorientation angle threshold assuming that grains are objects enclosed by boundaries which fulfill the segmentation criterion at every point along the boundary (here, a minimum angle of misorientation of 10° is chosen). In MTEX, the measurement points do not have to be located on a regular grid, although they usually are, nor do they have to be in direct contact with one another. It is possible to reconstruct grains which are dissected by arrays of non-indexed pixels (e.g. scratches)

Solid Earth Discuss., doi:10.5194/se-2017-30, 2017
Manuscript under review for journal Solid Earth
Discussion started: 20 March 2017

as long as the misorientation angle between the disconnected pieces is below a given threshold and spatial conditions are fulfilled (Bachmann et al, 2011) . It is also possible to attribute fractions of non-indexed pixels to the closest grain, i.e., to an indexed area, based on certain textural or spatial criteria. This procedure, in the following called grain completion, generates grain boundaries which outline 'completed' grains, i.e., grains consisting of indexed pixels and 'incorporated' areas. The degree of grain completion has to be adapted to the individual image quality, therefore, the process of grain completion needs to be supervised. The most conservative approach is to use no grain completion at all, at the other end of the spectrum is the total completion which leave no pixel unassigned. The resulting grain boundaries for segmentation based on total completion are shown in Figure 3a. Grain boundaries obtained without grain completion are shown in Figure 3b. In contrast to the grain boundary bitmaps obtained by image analysis such as the CIP method (Figure 3c), EBSD grain boundaries have zero thickness and in the case of grain completion, the grain sizes need not to be integer multiples of the step size.

3.2.2. Procedure to obtain CIP boundaries:

Segmentation is carried out using Image SXM and the Lazy grain boundaries (LGB) macro (Heilbronner 2000, Heilbronner & Barrett, 2014). The input consists of 8 c-axis misorientation images (MOI), calculated with respect to 4 external reference directions (X, Y, Z and parallel to the applied principal stress, at 45° between X and Y, see sample coordinates, Figure 2) and 4 internal reference directions corresponding to the 4 most prominent maxima in the pole figure. The MOIs are combined to a stack and resized by a factor of 2 (or 4) using nearest neighbour interpolation (NN) to preserve the calculated pixel values and to retain sharp boundaries.

The sequence of steps necessary to complete a segmentation are listed in Table 3 in the form of LGB keystrokes. Typically the contrast of each slice is optimized by histogram equalization [e]. Edge detection (Sobel operator) is preformed [o], and the 8 gradient images are OR added [z], keeping the maximum value (of the 8 gradient images) at each pixel. The resulting image is thresholded at a grey value between 25 and 50 according to visual impression, values that correspond to approximately 1.2 - 2.5° (c-axis misorientation). One or two rounds of thickening [t], skeletonizing [j] and pruning [i] are applied to obtain grain boundaries that are 1 pixel wide. Depending on

Solid Earth Discuss., doi:10.5194/se-2017-30, 2017
Manuscript under review for journal Solid Earth
Discussion started: 20 March 2017

the noise caused by misindexing, additional median filtering needs to be applied, during the segmentation, to the slices of the stack [u] or to the combined image [m].

To obtain the final grain map, the grain boundaries are thickened to a width of 2 pixels and the grain boundary map (black lines on white background) is inverted. At this point, the grain map (black segments) consists of all possible 'grains', including those that consist of a hole, dirt or a different mineral phase. This is so because grain boundary detection does not only detect high gradients between indexed pixels of different c-axis orientation, but also between indexed and non-indexed pixel. Such 'grains' of non-indexed pixels are excluded from future analyses. As will be shown in the next section, this is accomplished through 'Redirect sampling' and by analyzing the grain map together with the MASK image (i.e., the map of the indexed pixels). The resulting grain boundaries are shown in Figure 3c.

3.3. Construction of grain size maps

From the grain maps, grain size maps are derived. To this end, the Lazy Map Redirect macro (LMR, see Appendix) is employed. In Image SXM, the grain map (black segments) and the MASK (indexed pixels black, non-indexed white),the grain map is scaled spatially, the scale being determined by the EBSD step size and the NN magnification used for segmentation. The LMR macro uses the Analyze function to determine the area of each segment on the grain map and the corresponding indexing density on the MASK. From the area, the diameter of the area equivalent circle is calculated (see Heilbronner & Barrett, 2014, for how to best calculate the correct diameter of an area). Rejecting areas with an indexing ratio below 75%, the pixels of every valid grain are assigned a grey value (GV) corresponding to the value of the diameter. A cut-off value can be selected and the rainbow LUT is used to visualize small values in blue and values above the cut-off in red (Figure 4). Note that grain size maps are both scaled in X and Y (spatial coordinates of the image plane), and calibrated in Z (grey values).

The grain size maps of the deformed and dynamically recrystallized samples of regime 1, 2 and 3 have been 'dilated', i.e. a ranking filter has been applied to close the gaps formed by the 'empty' pixels of the grain boundaries.

Solid Earth Discuss., doi:10.5194/se-2017-30, 2017
Manuscript under review for journal Solid Earth
Discussion started: 20 March 2017

3.4. Determination of mean grain size

The 2-D diameter of each segment is calculated from the cross sectional area (as mentioned above). The number weighted distribution h(d) of area equivalent diameters is presented as a histogram, for which the arithmetic mean, the mode, etc. can be determined. In order to be able to plot the data on the piezometer of Stipp & Tullis (2003), the root-mean-square (RMS) is calculated. Note that the RMS is biased towards the upper end of the distribution (larger grain sizes) and returns a value greater than the arithmetic mean. Because the RMS depends strongly on the tail end of the distribution, the histogram has to be cropped carefully to the relevant size range if the RMS is to be a meaningful measure of 'the' grain size.

To obtain a possible parent distribution of 3-D grains, the program stripstarD (Fortran source stripstarD.f and Matlab script stripstar.m, see Suppplementary Material) is used (details in Heilbronner & Barrett, 2014). The mode of the volume weighted histogram of 3-D diameters, v(D), is found by fitting a Gaussian, the mean of the Gaussian representing the mode of v(D) (Figure 5). Note that the mean is centered about the mode of v(D) and therefore independent of the long tail end of the distribution. In many instances, volume weighting is considered to be physically more meaningful than number-weighting because it is the mass of a certain grain size fraction that matters, not the number of grains in it. All 3-D and 2-D grain sizes evaluated for this study, i.e., the modal values of v(D) and the RMS of h(d) are listed in Table 4. In the following, the term '3-D mode' will refer to the mode of v(D), and the term '2-D RMS' to the RMS of h(d), being measures of 2-D and 3-D grain size respectively.

3.5. Extracting texture components

For the following investigation, the concept of a ‘texture component’ is not based on the full crystallographic information, i.e., defined by all three Euler angles, instead it refers to aspects of c-axis orientation only. Areas within orientations maps with a given texture component will be called domains. To construct a domain map, the c-axis misorientation image (MOI) is used. This image is thresholded at a level corresponding

Solid Earth Discuss., doi:10.5194/se-2017-30, 2017
Manuscript under review for journal Solid Earth
Discussion started: 20 March 2017

to the desired opening angle about the reference direction of the MOI (which is defined on the pole figure), i.e, about the central c-axis orientation of the domain. Each of the domain maps shown in Figure 6 and c is created by superposing a mask made from the MOI, thresholded at 15° (for a 30° opening angle), on the c-axis orientation image with a continuous color coding of 360° of azimuth (AZU CLUT). The CLUT is shown as a background to the pole figures in Figure 6a.

In the paper by Heilbronner & Tullis (2006), a number of c-axis maxima and domains are identified. Their names allude to the slip system whose activity was supposed to give rise to them (e.g. Schmid & Casey, 1986). The 'prism' domain, with c-axes parallel to the structural Y-direction, indicative of prism <a> slip, the 'basal' domain, with c-axes on the periphery, slightly rotated from the structural Z direction in the sense of shear, indicative of basal <a> slip, the 'rhomb' domain, with two symmetrically disposed c-axis maxima on the inclined girdle, oriented for rhomb <a> slip, and the 'σ_1'domain, with a c-axis maximum on the periphery, oriented in the 'hard' direction, i.e., parallel to the direction of the applied load. Here, the names for the domains are Y-domain, B-domain, R-domain and σ_1-domain, respectively (see Figure 6, inset upper right), but without implicitly assuming that a specific c-axis orientation implies the activity of a certain slip system .

3.6. Maps of misorientation density

To investigate the conspicuous grain size gradient of the regime 1, 2, 3 samples shown in Figure 4, the internal misorientation density is determined by a method described in detail in the companion paper (Kilian & Heilbronner, same volume) and mapped as shown in Figure 7. Briefly, a higher-order kernel average misorientation (KAM) is calculated on orientation-noise reduced EBSD data, and for each grain, the sum of the KAM is divided by the number of measurements, providing the grain averaged KAM (gKAM). The gKAM represents an estimate for the intragranular density and the misorientation angle of low angle boundaries.

Solid Earth Discuss., doi:10.5194/se-2017-30, 2017
Manuscript under review for journal Solid Earth
Discussion started: 20 March 2017

4. Results

4.1 Grain size of dynamic recrystallization regimes

The 2-D grain size distribution is visualized using grain size maps (Figure 4). A few aspects in this figure merit attention. Comparing the predominant colours of the grain size maps with this CLUT suggests that the cross sectional areas of most of the grains of the regime 1 samples have diameters of less than 5 μm, those of regime 2 less than 8 μm and those of regime 3 less than 15 μm. In addition, a rather clear grain size gradient can be recognized for w946.

Expressed in terms of the 3-D mode, the grain size of the starting material (undeformed BHQ) is 104 μm, which is much larger than the recrystallized grain size (as shown in Figure 5, inset). The recrystallized grain size for the seven samples deformed in regime 1, 2, and 3 to high and low total shear strain is shown in Figure 5. The modal values found for the sample w1092, w946 and w935 shown as grain size maps in Figure 4 are 4.1 μm, 6.5 μm, and 14.7 μm, respectively, values that coincide with the visual impressions of <5 μm, <8 μm and < 15 μm. Note that the corresponding RMS values 3.4 μm, 4.5 μm and 9.4 μm (Table 4a), do not fit the visual impression as nicely. The high strain samples are almost completely recrystallized. The same is not true for the low strain samples, and accordingly, their distributions v(D) are not strictly monomodal, and rather show quite a number of grains at the larger end of the histogram.

4.2. Identification of subdomains

Upon closer inspection, the pole figures reveal that the maxima of the Y- and B-texture components are usually composed of two distinct submaxima. Selecting these ('upper' and 'lower') submaxima in a pole figure, two separate orientation images for the corresponding texture component, i.e., two subdomains can be created (Figure 6). What was originally considered one Y- or one B- domain, is actually composed of two non-intersecting spatial domains as evidenced by the different colours which highlight the distinct ranges of azimuth of c-axis orientations of each of the subdomains (compare Figures 6b and 6c).

Solid Earth Discuss., doi:10.5194/se-2017-30, 2017
Manuscript under review for journal Solid Earth
Discussion started: 20 March 2017

379

380 4.3. Grain size of domains and subdomains

381

382 The grain size analysis for the Y-domain of sample w935 (regime 3) and its
383 subdomains is shown in Figure 8. The histograms below the maps are obtained by
384 grouping the grey values (which are calibrated to the 2-D diameter of the grains). The
385 mean value of the histograms represents the arithmetic mean of the area-weighted size
386 distribution a(d). This means, for example, that in the case of the Y-domain of w935,
387 the mean area fraction is occupied by grains of 14.2 µm diameter, i.e., 158 μm^2 cross
388 sectional area. The mean values of a(d) always lie between the 2-D RMS and the 3-D
389 mode. Thus, for the same domain, RMS = 9.6 µm < 14.2 µm < 3-D mode = 16.0 µm (see
390 also Table 4c). The area weighted distribution of diameters is not to be confused with
391 the frequency distribution of areas, which, for the same domain, has an arithmetic
392 mean of 247μm^2 corresponding to a diameter of 17.7 µm.
393 The grain sizes of the (combined) B- and Y-domains have been calculated for the
394 high strain samples in regime 1, 2, and 3 (Figure 9). The ratio between the
395 recrystallized grain size of the Y-domains and the bulk grain size is > 1.00 for sample
396 w935, ≈ 1.00 for samples w965 and w946, and < 1.00 for sample w1092. Conversely,
397 the ratio between the recrystallized grain size of the B-domains and the bulk grain size
398 is > 1.00 for samples w965, w946 and w1092, and < 1.00 only for sample w935 (see
399 also Table 4c). This point is also taken up in the companion paper (Kilian &
400 Heilbronner, same volume).

401

402 4.4. Grain size and misorientation density

403

404 To explore the relation between grain size and the state of deformation (as
405 indicated by misorientation density) the grain maps are evaluated separately for high
406 and low gKAM regions (Figure 7). The 3-D modes are determined for the upper and
407 lower halves of the samples w1092 (regime 1) and w946 (regime 2), and in four strips
408 of sample w935, results can also be found in Table 4b. Clearly, regions of higher gKAM
409 have a smaller recrystallized grain size and regions of lower gKAM have a larger
410 recrystallized grain size. Obviously, non-recrystallized grains also show high gKAM
411 values but (due to their low frequency) are not considered in this analysis.

Solid Earth Discuss., doi:10.5194/se-2017-30, 2017
Manuscript under review for journal Solid Earth
Discussion started: 20 March 2017

412
413 4.5. Grain size and flow stress
414
415 Finally, the grain size data are plotted on the piezometer of Stipp & Tullis (2003).
416 The results are presented in two types of plots in Figure 10: in the top row 3-D modes
417 are used for the diameter, in the bottom row, the corresponding 2-D RMS values are
418 plotted to fit the piezometer data set. On account of the high volume fraction of
419 recrystallized grains (≥ 90%), the high strain samples are considered the most reliable
420 data points and plotted separately (Figure 10a). In view of the grain size gradient
421 across the samples w1092, w946 and w935 (see Figure 4), both the minimum and
422 maximum grain sizes are shown, the line fit considers all 6 data points. The picture
423 does not change fundamentally, if the low strain samples are included (Figure 10b).
424 Finally, two slightly different line fits are obtained for the recrystallized grain sizes of
425 the Y- and B-domains (Figure 10c).
426
427
428
429

Solid Earth Discuss., doi:10.5194/se-2017-30, 2017
Manuscript under review for journal Solid Earth
Discussion started: 20 March 2017

5. Discussion

5.1 Confirmation of CIP results with EBSD analysis

Processing and representing the EBSD mapping as c-axis orientation images (COI), shows that both methods, EBSD and CIP, coincide down to the limit of optical resolution of polarization microscopy (Figure 11). The maps are very similar, and the geometry c-axis pole figures are very similar, differences being due to a number of circumstances. Firstly, the SEM penetrates a small layer near the surface of the thin section whereas the CIP method works in transmission. In optical light microscopy, information from the entire thickness of the thin section contributes to the result, and, even more importantly, grain boundaries appear as a separate phase of isotropic (dark) material, and thus disturb the analysis of the nearby pixels, especially if the grain boundaries are orientated at a low angle to the section surface. A second source for differences between EBSD and CIP are different procedures by which orientations are calculated from the input, a critical issue being the determination of c-axis inclinations in CIP.

The c-axis pole figures obtained by CIP and EBSD methods also compare very well (Figure 11). It came as a surprise that full texture analysis confirms that the so-called 'basal' and 'prism' maxima of c-axes are actually composed of two distinct submaxima. Previously, when doing the CIP analysis, it was always considered a problem of not being able to properly calibrate the inclination of the c-axes, if the B-maximum did not appear exactly on the periphery and if the Y-maximum did not occupy one position (rather than two) at or near the center of the pole figure (as shown Figure 11 for sample w965). However, the misorientation images (MOI) and grain size maps confirm this very clearly (Figures 6 and 8).

5.2 New insights through EBSD analysis

It is interesting to note that the Y-domain and the B-domain are arranged as layers with clusters of grains belonging to one or the other sub-maximum in the pole figure (see, e.g., Figure 8). Testing the neighbourhood relations between grains of the sub-maxima (using the spatial analysis described in chap. 18 of Heilbronner & Barrett,

2014) revealed that they are not randomly arranged within the layers but rather strongly clustered (Figure 12a). Pole figures with double Y-maxima have been shown repeatedly in a number of publications, however, no particular attention has been given to them (see e.g., Manktelow, 1987, Stipp et al., 2002, Mancktelow & Pennacchioni, 2010, Pennacchioni et al., 2010, Law, 2014).

In order to determine the shape of texture domains, the autocorrelation function (ACF) is used. Superposed lines on the ACFs (Figure 12b) represent the orientations of the 30% contours. Their trend with respect to the shear direction is 22° and 21° for the upper and lower subdomain, respectively, and 10° for the combined Y-domain. Obviously, the shallow trend of the Y-domain is the result of an imbricate arrangement of the more steeply inclined subdomains. On account of the shallow trend of the Y-domain, Heilbronner & Tullis (2006) argue, that while all domains deform as particles of higher viscosity in a low viscosity matrix (using the approach by Gay, 1968), yet the 'prims' domain is the one with the lowest viscosity ratio (R) of them all, having $R \approx 2$ (where $R = \mu / \mu_0$, μ being the viscosity of the domain and μ_0 the viscosity of the matrix) making it the 'softest' among all domains.

In this contribution, however, we prefer not to pursue the approach by Gay because of the shortcomings and errors associated with it. Instead we first calculate an Rf-phi diagram with the aspect ratios and orientations of the Y-subdomains based on a procedure described by Mancktelow (2011) based on Bilby and Kolbuszewski (1977). Next, we calculate the finite strain of the bulk sample assuming homogeneous continuous general shear according to Tikoff & Fossen (1993). And finally we calculate the ACF of the domain and subdomain clusters from which we derive the aspect ratio and orientation (Rf-phi coordinates). Plotting these values into the Rf-phi diagram reveals that, the subdomains plot on the equiviscous curve (R = 1), as does the bulk sample by default, while the full domain plots on a curve for a viscosity ratio >1. Note,that the shear strains of the subdomains remain about 1/3 ofare significantly lower ($\gamma \sim 1$) than the strue shear strain for the bulk sample w935 with a ($\gamma \sim 3$) implying that subdomains deform at a lower rate than the bulk sample, while they still are iso-viscous with respect to their neighboring domains. Such a situation however, requires an additional strain producing and accommodating mechanism operative throughout the entire sample, a possible candidate being grain boundary sliding. Grain boundary sliding has been suggested for regime 1 experiments (Stipp & Kunze, 2008;

Kidder et al., 2016) however, that it could also contribute to bulk strain in regime 2 and 3 was not suspected.

Another interesting point to note is the ratio of the apparent shear strain, usually reported as γ in deformation experiments (see Figure 1), to the effective shear strain $\gamma_{effective}$ of ~1.6 (see Table 1). When comparing experimental microstructures to natural ones, the question arises which experimental γ-value should be used for comparison with the shear strain measured in the field.

A number of alternative measures derived from the initial and the final thickness of the shear zone (Gleason & Tullis, 1993) or methods for the incremental calculation of shear strain (Richter et al., 2016) have been proposed. Like the true shear strain and the effective shear strain, all of these measures return smaller values, which may be closer to values that are relevant in nature. Using the apparent shear strain (the highest possible) may be part of the reason why in nature a steady state microstructure and texture appears to be established at much lower strains than in experiments, (see discussion by Pennacchioni et al., 2010). It also means, that care should be taken when using the relation between volume fractions of recrystallized grains and the (so-called) shear strain, as determined from general shear experiments, to estimate the shear strain in nature (Rahl & Skemer, 2016).

To assess the size of the subdomains we consider the ACF again. The long diameters of the 30% contours (typically used for size estimates, see Barrett & Heilbronner, 2014, chap. 20) are 59 µm, 64 µm and 153 µm, those of the 20% contours 103 µm, 111 µm and 356 µm, again for upper, lower subdomain and combined Y-domain, respectively. Both measures indicate that the cluster size of the combined domain is approximately 3x the cluster size of the subdomains. This led Heilbronner & Tullis (2006) to the conclusion that the 'prism' domains could not represent original BHQ grains (of 'prism' orientation) but must have grown by coalescence of preferentially replacing 'harder' 'basal' and 'σ_1' grains by 'softer' 'prism' grains through preferred recrystallization and coalescence. - Considering now, that the subdomain clusters have abut the same diameters as the original BHQ grains and that their orientation is compatible with strain, another interpretation is possible: subdomain clusters could indeed be the strained 'ghosts' of the original BHQ grains, with strain by a crystal plastic mechanism bringing their c-axes close to a common Y- direction but never into parallelism. The co-existence of such intercalated subdomains, in particular,

the a-axis alignment and low 'transparency' (simplified m'-factor) at their boundaries is investigated in more detail in the companion paper (Kilian & Heilbronner, this volume).

The misorientation density as measured by the gKAM can be interpreted as a indicators of deformation intensity - in the case of subgrain rotation recrystallization. Thus, highly deformed (recrystallized) grains should have high gKAM values. However, whether or not a grain is highly deformed may depend on its crystal orientation with respect to the kinematic framework. In the companion paper (Kilian & Heilbronner, this volume) this correlation is explored. Comparison of the grain size maps (Figure 4) with the maps of grain kernel average misorientation (gKAM) (Figure 6), shows that regions with high overall gKAM values are also regions of overall smaller grain size. Gradientsof grain size and gKAM may not always be as well developed as in the samples shown in Figures 4 and 7. The absence of such gradients is probably the result of homogeneous deformation of the sample (across the entire width of the shear zone) whereas gradients point to strain and possibly stress concentrations. This point will be taken up later.

For regions with constant gKAM, however, the size ratios between texture domains persist, as can be seen by comparing the map for the Y-domain and that for the non-Y domain in Figure 8. They both show an overall size increase from top to bottom, but at every level on that traverse, the Y-domain shows larger grain sizes than the non-Y domain. For sample w935 (shown in Figure 8), the ratio between Y- and non-Y domain is ~1.2, while for w965 (not shown), the same ratio would be ~1.0, keeping in mind that this may also be an effect of lower indexing ratios in the non-Y-domain. In other words, while the overall recrystallized grain size is inversely correlated to the level of the gKAM, the gKAM itself does not give rise to the grain size difference between different texture domains.

5.3 Methods of segmentation: how to find the correct grain boundaries

To obtain a grain or particle size distribution (GSD or PSD), the individual grains must be identified, and a grain map or a grain boundary map has to be constructed. This operation is called segmentation, and there are a number of ways of achieving it: by tracing the boundaries manually, or by letting the computer do the work, for

Solid Earth Discuss., doi:10.5194/se-2017-30, 2017
Manuscript under review for journal Solid Earth
Discussion started: 20 March 2017

example, by identifying coherent grains on the basis of parallel crystal orientation, by recognizing grain boundaries as sharp changes of crystal orientation or by solving a minimization problem on orientation variance. For manual tracing of grain boundaries, we use the human visual systems with its inbuilt intelligence and its well trained biases (concerning the shape of objects and outlines, for example). It is commonly considered the most reliable way of recognizing objects and we implicitly make use of it when we inspect the result of a given segmentation (for example, in Figure 3), in order to judge whether it correctly portrays what we see on the map. In the following, the three types of segmentation described previously will be compared: 'CIP' denoting segmentation of the EBSD maps using c-axis orientations only, while 'EBSDnc' and 'EBSDc' denote segmentations of EBSD maps in full texture space, without any grain completion, and with partial, supervised completion respectively.

For the CIP segmentation, 8 misorientation images (MOI) were used as described above. On account of the histogram equalization carried out to enhance to contrast in the MOIs, the effective cut-off angle for the definition of a grain boundary is difficult to assess. Comparing the thresholded gradient images to the corresponding orientation gradient images (OGI) showed that the cut-off angle is approximately 1/20 of the thresholding level, and thus, that a minimum c-axis misorientation angle of 1.2° to 2.5° defines a grain boundaries (see Table 3). Sometimes this leads to low angle boundaries being classified as grain boundaries (see Figure 3c, right arrow). There is a simple reason for not using the OGIs directly, although they might be considered the more obvious choice. Compared to MOIs, the OGIs are noisy, smallest differences in c-axis orientation within a grain give rise to a gradient which may not be much lower than the minimum gradient defining the actual boundary. If the gradient images of 8 MOIs are combined, the signal-to-noise ratio is much lower. If light optical input is used for the calculation of the MOIs and OGIs, the OGIs cannot be used at all for segmentation, because of additional noise sources (as described by Heilbronner & Barrett, 2014).

It is to be expected that the difference between CIP and EBSD segmentations also depends on the level of indexing (Figure 3). For 100% indexing, all three types of segmentations (CIP, EBSDc and EBSDnc) are expected to yield the same result, provided that grain boundaries defined by misorientations about [0001] (which the CIP method cannot detect) are absent, and the criteria for the definition of a grain boundary (versus subgrain boundary) are the same. If a low indexing ratio is due to

Solid Earth Discuss., doi:10.5194/se-2017-30, 2017
Manuscript under review for journal Solid Earth
Discussion started: 20 March 2017

holes or dust particles, the CIP and EBSDnc approaches are expected to be more suitable because they avoid incorporating 'foreign phases' into grains (as shown in Figure 3a, left arrow). In these situations, grain completion must be supervised. If low indexing is due to poor pattern quality, however, EBSDc is probably more suitable, because it can merge grains that are dissected by patches of non-indexed pixels. Comparing the three segmentations in Figure 3, the first impression is that the grain boundaries of the EBSD and CIP segmentations coincide very well, in particular the EBSDnc segmentation that did not include grain completion is strikingly similar to the CIP segmentation by producing the same holes and gaps.

CIP and EBSD segmentations were tested on a number of samples. The result was always the same, irrespective of the level of indexing: the resulting grain size of the CIP method was smallest, followed by the EBSDnc, and the largest grain size returned by the EBSDc. In EBSD segmentation the misorientation angle used is the widely used value of 10° while the c-axis angle in CIP is much smaller, <3° (compare Table 3) . Using an angle of 5° for the EBSD segmentation, however, would re-produce the CIP grain sizes. Comparative histograms of 2-D diameters of CIP versus EBSDc and EBSDnc and values for the 2-D RMS and 3-D mode values are shown in Figure 13. That grain completion leads to a larger grain size is not surprising, as it allows to incorporate non-indexed pixels into the grains. However, the indexing ratio alone cannot account for the differences in segmentation. Another reason for the consistently larger grain size found by both EBSD methods lies in the clean-up procedure which removes single pixel grains, leaving the smallest grain size class empty (see, for example, the histograms of w935 in Figure 13). However, with the differences proving to be small and consistent, especially with respect to the mode(D) (see Table in Figure 13), and in order to use a homogeneous data set, the ensuing analyses were all based on CIP segmentation.

5.4 The recrystallized grain size in dislocation creep

There is a notion that grain size distributions can be described by a characteristic size, if they are monomodal, or by a characteristic size ratio, if they are fractal. In the context of dynamic recrystallization, and with an eye towards piezometric interpretations we are looking for a characteristic or average grain size. Recrystallized grain size piezometer relations can be written as $d = A \cdot \sigma^k$ or $\log(d) = A + k \cdot \log(\sigma)$

(Twiss, 1977; Poirier, 1985), where d stands for this average grain size, if the recrystallized grain size is assumed to be in a steady state during dynamic recrystallization and independent on temperature (e.g. Poirier & Guillopé, 1979; Shimizu, 2008). However, finding this grain size is not trivial, mostly because what we see of the grain size distribution is a 2-dimensional section of it. One option is to use the 2-D size distribution and determine a characteristic measure for the grain size from it, the other, to convert the distribution of sections to a distribution of 3-dimensional grains and determine a characteristic measure form it. Here, both the 2-D and the 3-D grain sizes were determined, the former because the results are to be compared against the piezometer of Stipp & Tullis (2003), the latter because it depends less on the shape of distribution than the former, thus providing a more reliable measure.

To assess grain growth during annealing, Heilbronner & Tullis (2002) performed gain size analyses (of the same samples that are re-analyzed here). Using a much coarser binning (limited by an old version of the stripstar program), they published histograms of v(R), where v is the volume weighted distribution and R the radius of the volume equivalent spheres. Maximum frequencies of regime 1, 2, and 3 samples occurred in the 2-4μm bin (w940), 2-4μm bin (w946) and 6-8μm bin (w935 and w920), the estimated modal 3-D diameters are given as 7 μm, 8 μm, and 14 μm. The values for regime 3 are confirmed by the present study, which yields a value of 14.7 μm (w935). As the regime 1 and 2 grain sizes are too small to be properly resolved by the CIP method, it is not surprising that the grain sizes found with EBSD are smaller, with values of 5.3 μm (w940) and 6.5 μm (w946) (Table 4a).

In their study on texture evolution in regime 3 dislocation creep, Heilbronner & Tullis (2006) found that the recrystallized grains in the 'prism domain' (here Y-domain) are larger than grains of other domains. Considering inverse grain boundary density (Figure 12c in Heilbronner & Tullis, 2006), the size ratio between the recrystallized grains in the Y-domains compared to the average reaches a value of ~1.4 at high shear strains. The same figure also predicts that the ratio for the so called 'basal domain' (here B-domain) should attain a value of 1.0 or even <1.0. To check these claims for regime 3, and to check if they also apply to regime 1 and 2 samples, maps of texture domains were prepared and the grain size of the Y- and B- domain determined (Figures 8 and 9). For regime 3, it is found that the 3-D mode of the recrystallized grains of the bulk is 14.7 μm, that of the Y-domain 16.0 μm and that of the non-Y

Solid Earth Discuss., doi:10.5194/se-2017-30, 2017
Manuscript under review for journal Solid Earth
Discussion started: 20 March 2017

661 domain 13.4 μm (sample w935, Figure 8). However the ratio of the recrystallized grain
662 size in the Y-domain to the average is only 1.1 (w935) and 1.01 (w965), while the ratio
663 of the B-domains to the average is 1.0 (w935) and 1.05 (w965) (Figure 9). In other
664 words, the expectation that Y-domains in regime 3 have a larger recrystallized grain
665 size and B-domains an average or smaller grain sizes is confirmed, if not to the full
666 extent of the predictions made in 2006.
667 Note that for the study presented in the paper by Heilbronner & Tullis (2006) the
668 available data base was not sufficiently large and the method of size estimation via
669 grain boundary density not well enough calibrated to allow for a quantitative
670 prediction. Nevertheless, it could be documented that the relative size of the
671 recrystallized grains of the 'prism', the 'basal' and other domains evolve continuously
672 with increasing shear strain. In this study another interesting point emerges: the ratio
673 between the recrystallized grain sizes in the different domains depends on the regime
674 and may change depending on the stress level. For regime 1 and 2, the size ratios of the
675 recrystallized grains in the Y- and B- domains with respect to the average can also be
676 extracted from Figure 9. Proceeding from the strongest to the weakest sample (regime
677 1 w1092, regime 2 w946, regime 3 w965 and w935), the size ratio for the Y-domain is
678 0.95, 1.0, 1.0, 1.1, and for the B-domain 1.1, 1.1, 1.05, 0.97, respectively. The resulting
679 stress dependence of the recrystallized grain size in the Y- and B-domain are shown in
680 Figure 10c. In view of the subtle difference between the two and the possible errors
681 associated with the stress determinations, it is not clear if this result, however
682 provocative, is significant at all - it certainly merits an additional study.
683
684 5.5 Dependence of grain size on stress
685
686 When the dislocation creep regimes were introduced by Hirth & Tullis (1992),
687 the regimes 1, 2 and 3 were defined by the microstructure. At the same time, the
688 boundaries between the regimes were observed to be constant stress boundaries,
689 placing regime 1 above a differential stress, $\Delta\sigma$, of 400 MPa, regime 2 at approximately
690 300 MPa and regime 3 at or below 200 MPa. For shear experiments, these values
691 translate to shear stresses, τ, of 200 MPa, 150 MPa, and 100 MPa, respectively, values
692 that were realized, e.g., in the studies of Heilbronner & Tullis (2002 and 2006). The
693 stress-strain curves of the samples analyzed here (Figure 1b) also confirm this trend to

close approximation. Only the low strain sample of regime 2 (w1086) deforms at a higher shear stress than the low strain sample of regime 1 (w940), raising the question whether w1086 should not better be counted as regime 1.

When plotting the recrystallized grain sizes against differential stress, the high strain samples follow a clear trend (Figure 10a), however at higher stress levels than predicted by the quartz piezometer of Stipp & Tullis (2003). Including the low strain samples does not significantly alter the picture (Figure 10b). If a curve is fitted through the data, again, higher stresses or higher grain sizes would be predicted compared to the piezometer. In the case where the grain size is given as the 3-D mode (red curves in Figure 10), this is to be expected because the 3-D mode is always larger than the 2-D RMS for which the piezometer was calculated. But the curves fitted to the 2-D RMS values (green curves in Figure 10) also yield higher stresses or grain sizes.

Where does this discrepancy come from? A number of explanations are possible. Heilbronner & Tullis (2006) attributed the higher stresses to the use of a solid confining medium as compared to the molten salt assembly that had been used for the piezometer experiments. If the correction proposed by Holyoke & Kronenberg (2010) were to be used, the curve fit would shift to lower stresses but still remain significantly above the piezometer. However, this correction was not used for the re-calculation of the stress strain curves because without it, the new rig software achieved correct stresses as 'calibrated' against the quartz-coesite transition (Richter et al., 2016).

Comparing general shear experiments to axial shortening ones requires a conversion of shear stress to differential stress. Lower differential stresses could result if, instead of the Mohr circle construction, $\Delta\sigma = 2 \cdot \tau$, smaller conversion factors could be used. For torsion experiments, $\Delta\sigma = \sqrt{3} \cdot \tau$, (Paterson & Olgaard, 2000), and if the stress exponent n is considered, using $\tau = 3^k \cdot \Delta\sigma$ (where $k = -(1+1/n)/2$), a range of values from $\Delta\sigma = 3 \cdot \tau$ (for n=1) and $\Delta\sigma = \sqrt{3} \cdot \tau$ (for n >>1) is possible (Ranalli 1987; Schmid et al, 1987). In other words, none of these theoretically possible conversion factors produces an acceptable overlap of the curve fits and the piezometer.

Note that the line fit for the 2-D RMS data (Figure 10b) is approximately parallel to the regime 1 piezometer (grey line). If the shear stress is used directly ($\Delta\sigma = \tau$), the curve fit intersects the regime 2&3 piezometer (black line) between the regime 2 and 3 data points, the point being close to the regime 2&3 piezometer, but parallel and above the regime 1 piezometer. This raises the question if the regimes and regime boundaries

of the general shear experiments correspond one-to-one to those of the axial shortening experiments. However, because more data would be needed to explore the implications of this observation, this line of arguments is not pursued any further here.

The piezometer experiments were conducted to relatively low finite strains and were stopped long before 100 % volume fractions of recrystallization was achieved. However, including low strain experiments (Figure 10b) shows that the mismatch cannot be due to different amounts of recrystallization. An interesting question is whether the piezometer relation is restricted to coaxial progressive deformation deformation and does not apply to non-coaxial progressive deformation, however, the answer to this question is again outside the scope and focus of this study.

Irrespective of the absolute stress levels of the experiments discussed here, a relation of misorientation density and recrystallized grain size can be documented. The stress-grain size relation (Figure 10a), is calculated using only the high strain and more or less fully recrystallized samples. In view of the grain size gradients across theses samples (Figure 4), and the relation of these on the grain averaged KAM (Figure 7), a low and a high gKAM site are used in each case. In all cases, lower gKAM values coincide with larger recrystallized grain size. While each pair is plotted for the shear stress determined for the sample, it is quite possible that the grain size gradient in fact indicates a strain rate gradient caused by the localization of the deformation into a narrow active zone and which may potentially result in a stress gradient. Progressive thinning of the samples has been used as an explanation for the apparent strain hardening at the end of long shear experiments (Heilbronner & Tullis, 2002). Raised stress levels may also occur at the grain scale, both in function of the crystallographic orientation of the grain with respect to the principal the kinematic framework, or at grain-to grain contacts as long as recrystallization is incomplete. It is therefore possible that shear stresses determined for bulk samples are different from the stress 'felt' by the actively deforming material.

Solid Earth Discuss., doi:10.5194/se-2017-30, 2017
Manuscript under review for journal Solid Earth
Discussion started: 20 March 2017

6. Summary and conclusions

A microstructure and texture analysis of 7 samples of Black Hills Quartzite, deformed experimentally in the dislocation creep regimes 1, 2 and 3, was carried out with the aim of comparing previously published data obtained by the CIP method to a renewed analysis making use of the higher resolution (both spatially and in terms of crystallographic orientation) of EBSD. Extended grain size analyses now include samples from regime 1 and 2. The stress strain data were re-calculated using an improved version of the rig program.

1. The c-axis orientation images and pole figures obtained by CIP and EBSD are practically the same, with the exception of the inclination which is a innate problem of the CIP method, and the segmentations using a the CIP and EBSD approach recognize the same grain boundaries, again with very few exceptions.
2. The Y-domain (identified previously as 'prism domain) is composed of two subdomains, the same is true of the B-domain ('basal' domain). The size of the subdomains corresponds to the original grain size of BHQ.
3. Grain size analysis shows that the recrystallized grain size of BHQ deformed in general shear experiments
   - depends on texture
   - depends on flow stress
   - does not depend the amount of total sample strain-or recrystallization
   - is inversely-correlated with misorientation density across samples with strain gradients
4. The recrystallized grain size of the Y- and B- domain may have different stress dependences.
5. The shape and grain size of the Y-subdomains suggests that they deform iso-viscous to the bulk experiment, but potentially to a lower shear strain than the bulk experiment, calling for an additional deformation mechanism other than dislocation creep.
6. The stress dependence of the grain size does not fit the piezometer of Stipp and Tullis (2003), which was produced from axial experiments, but predicts higher stress or higher grain sizes.

Solid Earth Discuss., doi:10.5194/se-2017-30, 2017
Manuscript under review for journal Solid Earth
Discussion started: 20 March 2017

793 Future work is suggested to examine whether the discrepancy between the grain
794 sizes obtained here and the published piezometer are only due to discrepancies
795 between the stress calculations for solid medium confining pressure as opposed to
796 molten salt assembly, as was used for the piezometer experiments. If so, this would
797 suggest that the stresses reported in the literature for experiments carried out with
798 solid medium confining pressures are too high by a factor of 2 or more. On the other
799 hand, it may indeed show that the co-axial and non-coaxial progressive deformation
800 produce different re-crystallized grain sizes.
801
802

Solid Earth Discuss., doi:10.5194/se-2017-30, 2017
Manuscript under review for journal Solid Earth
Discussion started: 20 March 2017

7. Acknowledgements

We are indebted to Jan Tullis who not only provided the samples of this study but who continues to contribute, in the generous fashion typical for her, to the advancement of microstructure and rock deformation studies. We wish to thank Willy Tschudin of Basel University for the preparation of excellent thin sections, Tom Eilertsen and Kai Neufeld of the Arctic University of Tromsø for their dedicated technical support and the time and effort spent during the acquisition of the EBSD maps. Michael Bestmann is thanked for always sharing his immense experience. The paper has further profited from discussions with Michael Stipp, Greg Hirth and Andreas Kronenberg. Support by the National Science Foundation of Switzerland, grant no. NF 200021-138216 (Deformation mechanisms in naturally and experimentally deformed minerals and rocks (9)) is gratefully acknowledged.

References

Bilby, B. A. and Kolbuszewski, M. L. (1977). Finite deformation of an inhomogeneity in 2-dimensional slow viscous incompressible-flow. Proc. R. Soc. London Ser. A-Math. Phys. Eng. Sci., 355(1682), 335–353.

Chernak, L. J., Hirth, G., Selverstone, J., and Tullis, J. (2009). Effect of aqueous and carbonic fluids on the dislocation creep strength of quartz. Journal of Geophysical Research-Solid Earth, 114:B04201.

Dellangelo, L. N. and Tullis, J. (1989). Fabric development in experimentally sheared quartzites. Tectonophysics, 169(1-3):1–21.

Gleason, G. C., Tullis, J., and Heidelbach, F. (1993). The role of dynamic recrystallization in the development of lattice preferred orientations in experimentally deformed quartz aggregates. J. Struct. Geol., 15(9-10),1145–1168.

Gleason, G. C. and Tullis, J. (1995). A flow law for dislocation creep of quartz aggregates determined with the molten-salt cell. Tectonophysics, 247(1-4),1–23.

Heilbronner, R. and Barrett, S. (2014), Image Analysis in Earth Sciences - Microstructures and Textures of Earth Materials. Spinger Verlag, Heidelberg, 520 pp. ISBN: 978-3-642-10342-1 (Print) 978-3-642-10343-8 (Online).

Heilbronner, R., and J. Tullis (2006), Evolution of c axis pole figures and grain size during dynamic recrystallization: Results from experimentally sheared quartzite, J. Geophys. Res., 111, B10202, doi:10.1029/ 2005JB004194.

Heilbronner, R. and Tullis, J. (2002). The effect of static annealing on microstructure and crystallographic preferred orientations of quartzites experimentally deformed in axial compression and shear. In: S. de Meer, M.R. Drury, J.H.P. de Bresser and G.M. Pennock (Editors), Deformation Mechanisms, Rheology and Tectonics: Current Status and Future Perspectives. Geol. Soc., Lond., Spec. Pub., pp. 191-218.

Heilbronner, R. (2000). Automatic grain boundary detection and grain size analysis using polarization micrographs or orientation images. Journal Structural Geology, 22: 969-981.

Hielscher, R. and Schaeben, H. (2008). A novel pole figure inversion method: specification of the MTEX algorithm, J. Appl. Crystallography, 41, pp. 1024-1037.

Hirth, G., and J. Tullis (1992). Dislocation creep regimes in quartz aggre- gates, J. Struct. Geol., 14, 145–159.

Holyoke, C. W., III, and A. K. Kronenberg (2010). Accurate differential stress measurement using the molten salt cell and solid salt assemblies in the Griggs apparatus with applications to strength, piezometers and rheology, Tectonophysics, 494, 17–31, doi:10.1016/j.tecto.2010.08.001.

Kidder, S., Hirth, G., Avouac, J.-P., and Behr, W. (2016). The influence of stress history on the grain size and microstructure of experimentally deformed quartzite. J. Struct. Geol., 83, 194–206.

Kilian, R. and Heilbronner, R. (subm.). Interrelation of creep processes and crystallographic preferred orientation in experimentally deformed Black Hills Quartzite. Solid Earth, this volume.

Law, R.D. (2014). Deformation thermometry based on quartz c-axis fabrics and recrystallization microstructures: A review. J. Struct. Geol., 66, 129-161.

Mancktelow, N., and G. Pennacchioni (2010), Why calcite can be stronger than quartz, J. Geophys. Res., 115, B01402, doi:10.1029/2009JB006526.

Mancktelow, N. (1987) Quartz Textures from the Simplon Fault Zone, Southwest Switzerland and North Italy, Tectonophysics, 135, 133-153.

Mancktelow, N. S. (2011). Deformation of an elliptical inclusion in two-dimensional incompressible power-law viscous flow. J. Struct. Geol., 33(9), 1378–1393.

Panozzo Heilbronner, R. and Pauli, C. (1993). Integrated spatial and orientation analysis of quartz c-axes by computer-aided microscopy. J. Struct. Geol., 15(3-5): pp. 369-382.

Paterson, M.S., Olgaard, D.L., 2000. Rock deformation tests to large shear strains in torsion. J. Struct. Geol. 22, 1341–1358

Pec, M., H. Stünitz, R. Heilbronner, and M. Drury (2016). Semi-brittle flow of granitoid fault rocks in experiments, J. Geophys. Res. Solid Earth, 121, 1677–1705, doi:10.1002/2015JB012513.

Pennacchioni, G., Menegon, L., Leiss, B., Nestola, F., Bromiley, G., 2010. Development of crystallographic preferred orientation and microstructure during plastic deformation of natural coarse-grained quartz veins. Journal of Geophysical Research-Solid Earth 115. DOI 10.1029/2010JB007674

Poirier, J. (1985). Creep of crystals: high-temperature deformation processes in metals, ceramics and minerals. Cambridge Univ Press, Cambridge.

Poirier, J. and Guillope, M. (1979). Deformation induced recrystallization of minerals. Bulletin De Mineralogie, 102(2-3), 67–74.

Post, A., Tullis, J., and Yund, R. (1996). Effects of chemical environment on dislocation creep of quartzite. Journal of Geophysical Research-Solid Earth,

101(B10):22143–22155.

Ranalli, G. (1987). Rheology of the Earth, 1st ed. Allen and Unwin, London.

Rahl, J. M. and Skemer, P. (2016). Microstructural evolution and rheology of quartz in a mid-crustal shear zone. Tectonophysics, 680, 129–139.

Richter, B., Stünitz H. and Heilbronner R. (2016), Stresses and pressures at the quartz-to-coesite phase transformation in shear- deformation experiments, J. Geophys. Res. Solid Earth, DOI: 10.1002/2016JB013084.

Schmid, S. and Casey, M. (1986). Complete fabric analysis of some commonly observed quartz c-axis patterns, Volume 36 of Geophysical Monograph, 263–286. American Geophysical Union.

Schmid, S., Panozzo, R., and Bauer, S. (1987). Simple shear experiments on calcite rocks - rheology and microfabric. Journal of Structural Geology, 9(5-6),747–778.

Shimizu, I. (2008). Theories and applicability of grain size piezometers: The role of dynamic recrystallization mechanisms. Journal Of Structural Geology, 30(7), 899–917.

Stipp, M. and Kunze, K. (2008). Dynamic recrystallization near the brittle-plastic transition in naturally and experimentally deformed quartz aggregates. Tectonophysics, 448(1-4):77–97.

Stipp, M., and J. Tullis (2003), The recrystallized grain size piezometer for quartz, Geophys. Res. Lett., 30(21), 2088, doi:10.1029/2003GL018444.

Stipp, M., Stünitz, H., Heilbronner, R. and Schmid, S.M. (2002) The eastern Tonale fault zone: a 'natural laboratory' for crystal plastic deformation of quartz over a temperature range from 250 to 700°C. Jour. Struct. Geol., v.24, pp.1861-1884.

Stipp, M., Tullis, J., and Behrens, H. (2006). Effect of water on the dislocation creep microstructure and flow stress of quartz and implications for the recrystallized grain size piezometer. Journal of Geophysical Research-Solid Earth, 111(B4).

Tikoff, B. and Fossen, H. (1993). Simultaneous pure and simple shear - the unifying deformation matrix. Tectonophysics, 217(3-4), 267–283.

Tullis, J., Christie, J., and Griggs, D. (1973). Microstructures and preferred orientations of experimentally deformed quartzites. Geological Society of America Bulletin, 84(1), 297–314.

Tullis, J. (1977). Preferred orientation of quartz produced by slip during plane strain. Tectono- physics, 39(1-3), 87–102.

Solid Earth Discuss., doi:10.5194/se-2017-30, 2017
Manuscript under review for journal Solid Earth
Discussion started: 20 March 2017

963 Twiss, R. (1977). Theory and applicability of a recrystallized grain-size
964 paleopiezometer. Pure and Applied Geophysics, 115(1-2), 227–244.
965
966

Solid Earth Discuss., doi:10.5194/se-2017-30, 2017
Manuscript under review for journal Solid Earth
Discussion started: 20 March 2017

Table Captions

Table 1

Mechanical data for general shearing experiments of Black Hills Quartzite.

1 Dislocation creep regime: 1, 2, 3; a, b = low, high shear strain
2 Sample number
3 Temperature
4 Minimum shear strain rate (at beginning of experiment, calculated from measured shearing and thinning of sample, for constant applied displacement rate)
5 Maximum shear strain rate (at end of experiment, calculated as above)
6 Confining pressure (confining medium NaCl)
7 Amount of water added
8 Shear stress at peak or yield
9 Steady state shear stress
10 Shear stress at end of experiment
11 Differential stress, calculated as $2 \cdot \tau_{flow}$
12 Displacement of forcing block parallel to 45° pre-cut
13 Thickness of sample at start
14 Thickness of sample at end of experiment
15 Apparent shear strain at end of experiment, as indicated on stress strain plots of shear experiments = (displacement along 45° pre-cut) / (final thickness of shear zone)
16 Effective shear strain = tan (Ψ) / k, where = shear angle (15), and k = th0 / thf

Table 2

EBSD data acquisition

1 Dislocation creep regime: 1, 2, 3; a, b = low, high shear strain
2 Sample name
3 Acceleration voltage
4 Probe current
5 Chamber pressure (Variable Pressure setting)
6 Aperture of beam
7 Working distance
8 Magnification
9 Speed of acquisition
10 Total recording time
11 Number of reflectors and number of bands detected
12 Mean value of MAD (mean angular deviation)
13 Hough resolution
14 Binning
15 Step size
16 Map size
17 Percentage of indexed measuring points

n.a. data not available
Recording dates:
dark grey AZtec 2.2, July 2014
light grey AZtec 2.3. March 2015
white AZtec 2.3 September 2016

Table 3

Image processing & segmentation
1 Dislocation creep regime: 1, 2, 3; a, b = low, high shear strain
2 Scanned maps
3 Method of image acquisition: EBSD = electron back scatter diffraction, CIP = computer integrated polarization microscopy
4 Size of EBSD map or CIP image used for analysis
5 Percentage of indexed pixels
6 Percentage of indexed pixels after correcting single misindexed pixel
7 Step size during image acquisition = pixel size of raw image
8 Type of image used for segmentation
9 Magnification (nearest neighbour interpolation)
10 Pixel size during segmentation
11 Segmentation procedure - key strokes of Lazy grain boundary and Lazy erode dilate macro
12 Minimal angular difference used to define a grain boundary

n.a. data not available
EBSD map obtained by electron back scatter diffraction
CIP map obtained by computer integrated polarization microscopy

Table 4

Grain size measurements.
1 Processed maps: prefix 1, 2, 3 indicates regime 1, 2, 3; a, b indicates low, high shear strain
2 Number of grains with >75% of pixels indexed
3 Mode of v(D) where v = volume weighted distribution and D = diameter of recalculated 3-D grains (volume equivalent spheres) = mean of Gaussian fit
4 Standard deviation of Gauss fit
5 Mean of Gaussian fit + 1 standard deviation = upper limit that includes 67% of population of 3-D grains
6 Upper limit including 84% of population of 3-D grains,
7 Upper limit including 99% of population of 3-D grains,
8 Root mean square of frequency distribution of diameter of 2-D sections h(d) where h = number density and d = diameter of 2D grains (area equivalent circles)

Solid Earth Discuss., doi:10.5194/se-2017-30, 2017
Manuscript under review for journal Solid Earth
Discussion started: 20 March 2017

1065 EBSDmap obtained by electron back scatter diffraction
1066 CIP map obtained by computer integrated polarization microscopy
1067 B-domain pixels with c-axis maximum at periphery of pole figure
1068 Y-domain pixels with c-axis maximum in center of pole figure
1069

Solid Earth Discuss., doi:10.5194/se-2017-30, 2017
Manuscript under review for journal Solid Earth
Discussion started: 20 March 2017

Figure Captions

Figure 1

General shear experiments on Black Hills quartzite.
(a) Simplified drawing of sample assembly for general shear experiments: 1 = confining medium (NaCl), 2 = axial load/ σ1 piston (Al2O3), 3 = forcing block (Al2O3), 4 = quartzite sample at 45° with respect to σ1 piston, 5 = furnace (carbon, pyrophyllite)
(b) Shear stress (τ) versus apparent shear strain (γ): blue = regime 1, green = regime 2, red = regime 3, stippled line = relatively low finite strain, solid line = relatively high finite strain (compare Table 1).

Figure 2

Orientation images.
(a) EBSD maps with color look-up tables (CLUT)
Euler RGB Euler coloring with Red = φ1, Green = Φ, Blue = φ2 (see CLUT).
IPFY, IPFZ Inverse pole figure coloring with respect to Y and Z (see CLUT).
(b) c-axis orientation images with look-up tables (LUT).
AZI, INC c-axis azimuth (0°-180°) and inclination (0°-180°) images calculated from Euler image, stereographic projection of LUT in upper right.
COI c-axis orientation image using Spectrum CLUT.
OGI c-axis orientation gradient image (EDG8a) showing average gradient with respect to 8 neighbours (see LUT).
MOI c-axis misorientation image: pixels with c-axis close to reference direction 0°/31° appear bright (see CLUT).
Upper right: c-axis pole figure, with (left-handed) XYZ sample coordinate system and coordinate system for c-axis orientation. Note that Z of this reference system is parallel to the structural Y direction. Scale bar and sinistral shear sense apply to all.
Detail of sample w965 is shown. For image processing, see text.

Figure 3

Segmentation based on texture.
Comparison of segmentations based on full texture (EBSD) and c-axis texture and shape (CIP).
From top to bottom:
Grain boundaries superposed on Euler RGB image, area with relatively low (~78%) indexing ratio. Arrow points to low angle grain boundary that is detected through structural filtering.
Area with relatively high (~94%) indexing ratio. Arrow points to segmentation artefact.
Frequency distributions, h(d), d = diameter of area equivalent circle: black = EBSD segmentation, grey = CIP segmentation, root-mean-square values are indicated.

Volume density distributions, v(D), D = diameter of volume equivalent sphere, derived from input h(d) using stripstar (see text), modal values are indicated.
(a) Segmentation using full texture assuming hexagonal symmetry of quartz and grain completion (see text).
(b) Same as (a) without grain completion.
(c) Segmentation using c-axis orientations only (see text).

Figure 4

Grain size maps.
Color coded grain size maps visualizing the diameter of area equivalent circles, d
From left to right: for undeformed Black Hills quartzite and samples deformed in regime 1, 2 and 3. Scale, shear sense, and look-up table for grain size apply to all. Red indicates the diameter of an area equivalent circle d ≥ 25 µm. Note, the diameter of undeformed Black Hills quartzite is ~ 100 µm.

Figure 5

Recrystallized grain size for dislocation creep regimes 1, 2, and 3.
Volume weighted histograms v(D) are shown for 7 samples for relatively low ($2.7 < \gamma < 4.3$) and high shear strains ($5.8 < \gamma < 7.1$).
D = diameter of volume equivalent sphere. The mode of v(D) is obtained by a Gauss fit to the distribution.
Note histograms with different size ranges: ($0 < D < 25$ µm) for regime 1 and 2, ($0 < D < 50$ µm) for regime 3.
Inset shows the grain size distribution of undeformed Black Hills quartzite for comparison.

Figure 6

Details of c-axis texture.
Color coded orientation images highlighting 'double maxima' c-axis orientations.
(a) Contoured polefigures superposed on the AZI color look-up-table (CLUT) used to highlight the azimuth of the c-axis orientation.
Inset Location of preferred orientations on the c-axis pole figure, proposed by Heilbronner & Tullis (2006): B ('basal'), R ('rhomb'), Y ('prism') and the direction of the axial load (at 45° with respect to the shear zone, usually inferred to be the direction of σ_1).
(b) Masked c-axis orientation images. Mask blocks all pixels with c-axis orientations outside a 30° cone (15° opening angle) about the reference direction. The reference direction is indicated below the image and corresponds to the upper maximum on the pole figure shown in (a).
(c) Same as (b) with the reference direction indicated below the image corresponding to the lower maximum on the pole figure shown in (a).

Solid Earth Discuss., doi:10.5194/se-2017-30, 2017
Manuscript under review for journal Solid Earth
Discussion started: 20 March 2017

Figure 7

Recrystallized grain size as function misorientation density.
Maps of grain kernel average misorientation (gKAM) are shown for 3 dislocation creep regimes. Maps cover nearly the full width of the shear zone. Gradients of gKAM are clearly visible. Modes of v(D) (size distribution of 3D grains) are calculated for high and low gKAM sites in samples w1092 and w946, and for 4 different sites of sample w935. Scale bar and color coding of gKAM apply to all.

Figure 8

Mapping grain size in texture domain.
Grain size maps of detail of sample w935 (regime 3) are shown. From left to right: showing all grains, grains in the upper and lower Y-subdomains, in the whole Y-domain and for c-axis orientations outside the Y-domain (see c-axis pole figure), same subdomains as in Figure 7. Domain maps are derived for c-axes orientations within a 30° cone (15° opening angle) with respect to the central orientation. Scale bar and shear sense apply to all.
Above maps:
Modes of v(D) are indicated above maps, where v = volume density distribution, D = diameter of volume equivalent sphere.
Below maps:
Histograms showing area weighted distributions of grain size (= grey value histogram of gain size map, see Heilbronner & Barrett, 2014 chap. 12), n = number of grains, mean = arithmetic mean of histogram. Note that the grain size in the Y-domains is larger than in the non-Y-domain, but the difference between upper and lower Y-subdomain is not considered significant.

Figure 9

Recrystallized grain size as function of texture.
Grain size distributions of recrystallized grains for four samples of regime 1, 2, and 3 of dislocation creep, arranged in 4 columns with c-axis pole figure above.
(a) Grain size distributions of all recrystallized grains.
(b) Grain size distributions of recrystallized grains with c-axis orientations within 30° cone (15° opening angle) about Y direction.
(c) Same as (b) for B direction.
Inset (upper left) shows location of c-axis orientations of B- and Y-domain on the pole figure.

Figure 10

Recrystallized grain size as function of flow stress.
Two measures of average grain size are plotted against differential stress, $\Delta\sigma$ (with $\Delta\sigma = 2 \cdot \tau$, see Table 1).

Top row: Mode of v(D), where D = diameter of volume equivalent sphere, and v = volume weighted frequency distribution (=3-D mode).
Bottom row: Root-mean-square of h(d), where d = diameter of area equivalent circle, and h = frequency distribution, as used for the piezometer relation by Stipp & Tullis (2003) (= 2-D RMS).
(a) High strain experiments ($5.8 < \gamma < 7.1$): in each case, higher value from low gKAM region, lower value for high gKAM region (see Figure 6).
(b) One measurement for each experiment (see Figure 1, Table 1).
(c) Grain sizes of Y- and B-domains (see Figure 7, 8)

Figure 11

Comparison of c-axis orientation images calculated with CIP from optical or EBSD derived input.
EBSD c-axis orientation image from EBSD input (SEM),
CIP c-axis orientation image from CIP input (polarization microscopy).
Spectrum CLUT for c-axis color coding, scale and shear sense apply to all.
With exception of w946, the exact same sampling sites are shown for each pair.

Figure 12

Spatial distribution and cluster size of Y-subdomains.
Results are shown for regime 3 sample w935.
(a) Spatial analysis to determine if spatial distribution of subdomains is random, clustered, or ordered (anti-clustered) :
Maps of subdomains with grain and phase boundaries are shown: 'upper' (green) and 'lower' (yellow) refer to the upper and lower maximum of the pole figure shown at right, scale bar below applies to all. On right: plot showing fraction of phase boundary surface (pb) and grain boundary surface (gb) versus volume fraction of the subdomains. Solid and stippled lines are the expected surface fractions for the random case. Fraction pb below and fractions gb above the expected values indicate significant clustering.
(b) Autocorrelation analysis of domain and subdomains: thresholded maps with autocorrelation function (ACF) below. Long and short diameters of contours in ACF reflect size and shape of clusters in domain and subdomain maps. Scale bar applies both to ACFs and maps. 3 contour levels are indicated as % of ACF_{max}. Superposed yellow lines indicate long diameter and orientation of 30% contour, black lines are extrapolations to 20% contour (see text).

Figure 13

Comparison of segmentations.
Frequency distributions h(d) are shown for regime 2 and 3. EBSD segmentations are plotted in black, corresponding CIP segmentation in gray.
(a) EBSD segmentation with grain completion
(b) EBSD segmentation without grain completion.

(c) Table with RMS of h(d) and modes of v(D), where d = 2-D diameter of area equivalent circle, D = 3-D diameter of volume equivalent sphere. Subscript 'c' = with grain completion, as in (a), subscript 'nc' = without grain completion, as in (b). RMS ratio CIP/EBSDc (%) = ratio of RMS values found by CIP versus EBSDc. Mode ratio CIP/EBSDc (%) = ratio of modes found by CIP versus EBSDc.

Figure 14

Relation of quartz domains and bulk sample strain.
Rf-φ type plot, calculated for general shear. Contours are for viscosity ratios μ/μ0 of 0.01, 0.5, 1, 2, 3, 6 and 9, calculated for the linear viscous case. Dashed lines = constant shear strain, black rhomb = bulk sample strain, red stars = Y-subdomains, grey star = entire Y-domain. Values for thickness th0, thf and displacement d are taken from Table 1. d/thf is the apparent shear strain (γ_a) reported for experiments. The effective shear strain $\Gamma = \gamma_a \cdot (thf/th0)$, the true shear strain $\gamma = 2 \cdot \gamma_a \cdot \ln(k)/(k^2-1)$. For the example of w935, the ratio of principal stretches R = 12.9 and the trend of the major axis of the strain ellipse Θ' = 7.5°. The kinematic vorticity number Wk = 0.92. Aspect ratios of the Y-subdomains are 2.5 and 2.7 and the corresponding trend of the long axes (ϕ) is 22° and 21°.Strain ellipses for bulk sample and Y-subdomains are shown on right. Note that the behaviour of a power law inclusions in a power law matrix (≠ linear viscous case) fits this plot only if μ/μ0 = 1, they do not fit the other contours - these are shown only to visualize the approximate trends of constant viscosity ratios.

Solid Earth Discuss., doi:10.5194/se-2017-30, 2017
Manuscript under review for journal Solid Earth
Discussion started: 20 March 2017

Solid Earth Discussions
Open Access
EGU

Table 1
Mechanical data for shearing experiments of BHQ

1	2	3	4	5	6	7	8	9	10	11	12	13	14	15	16
Regime	Sample	T (°C)	$\dot{\gamma}_{min}$ (10^{-5} s^{-1})	$\dot{\gamma}_{max}$ (10^{-5} s^{-1})	Pc (GPa)	H_2O (wt%)	τ(MPa) peak/ yield	τ(MPa) flow	τ(MPa) last	Δσ(MPa) for piezo	45°displ. (mm)	th0 (mm)	thf (mm)	total γ	$\gamma_{effective}$
1a	w940	850	1.46	2.50	1.50	-	413	238	238	476	3.60	1.27	0.87	4.1	2.8
1b	w1092	850	0.50	2.43	1.55	-	647	314	338	628	5.05	1.45	0.88	5.7	3.5
2a	w1086	875	1.33	2.60	1.58	-	269	300	294	600	2.49	1.14	0.87	2.9	2.2
2b	w946	875	1.04	3.08	1.50	0.17	220	201	265	402	4.44	1.24	0.65	6.8	3.6
3a	w1010	915	1.53	2.13	1.55	0.17	-	115	119	230	2.65	1.27	1.03	2.6	2.1
3b	w935	915	1.53	2.82	1.50	0.17	-	103	133	206	3.87	1.27	0.69	5.6	3.0
3b	w965	915	1.30	2.91	1.55	0.17	125	107	121	214	5.07	1.25	0.75	6.8	4.1

Solid Earth Discuss., doi:10.5194/se-2017-30, 2017
Manuscript under review for journal Solid Earth
Discussion started: 20 March 2017

Solid Earth Discussions
Open Access
EGU

Table 2
EBSD data acquisition

1	2	3	4	5	6	7	8	9	10	11	12	13	14	15	16	17
#	Sample	Voltage (kV)	Probe current (nA)	Pressure (Pa)	Aperture (µm)	WD (mm)	Magn.	Speed (Hz)	Time (h:m)	Reflectors / Bands	Mean MAD	Hough resol.	Binning	Step size (µm)	Map size (µm · µm)	Hit rate (%)
	undeformed material:															
	BHQ	20	5.3	35	120	9.48	200x	40.5	9:19	48 / 9	0.58	120	4x4	1.0	1388 · 980	91.4
	scanned sites of experiments:															
1a	w940	20	n.a.	2	120	14.5	250x	22.6	17:50	75 / 9	0.89	70	2x2	0.5	500 · 725	44.1
1b	w1092	20	n.a.	28	120	14.47	250x	22.8	18:45	75 / 10	0.90	110	2x2	0.5	550 · 700	92.8
1b	w1092-s30	20	n.a.	n.a.	n.a.	14.7	n.a.	11.2	10:48	75 / 9	0.81	70	2x2	0.5	241.5 · 452	77.3
2a	w1086	20	3.0	20	120	14.6	150x	22.6	5:54	75 / 9	0.90	70	2x2	0.5	600 · 200	72.0
2b	w946	20	n.a.	28	120	13.49	300x	22.8	18:16	75 / 10	0.62	110	2x2	0.5	750 · 485	94.3
3a	w1010-s34	20	9.0	25	120	14.3	200x	40.3	3:02	75 / 9	0.78	70	4x4	1.0	430 · 980	82.1
3a	w1010-s36	20	9.0	25	120	14.3	200x	11.4	2:51	75 / 9	0.84	70	2x2	1.0	500 · 830	78.5
3b	w935	20	n.a.	28	120	13.35	200x	22.8	15:58	75 / 10	0.57	110	2x2	0.9988	1275.5 ·1025.8	93.1
3b	w965-s40	20	6.0	25	120	15.0	150x	40.3	14:28	75 / 9	0.82	70	4x4	1.0	840 · 700	76.9
3b	w965-s45	20	3.0	20	120	148	250x	22.6	14:00	75 / 10	0.75	70	2x2	0.25	180 · 400	89.0

Solid Earth Discuss., doi:10.5194/se-2017-30, 2017
Manuscript under review for journal Solid Earth
Discussion started: 20 March 2017

Solid Earth Discussions
Open Access
EGU

Table 3
Image processing and segmentation

1	2	3	4	5	6	7	8	9	10	11	12
#	Map	Source	Cropped size (px)	Hit rate raw (%)	Hit rate deN (%)	Step size (µm)	Images used	Magn.	Pixel size (µm)	Procedure	Definition (°)
	BHQ	EBSD	1388 · 980	91.4	94.5	1.0	8 misors	1	1	LGB interactive	n.a.
	bhq 2.5x	CIP	1388 · 1040	-	-	2.439	nopol	1	2.439	visual boundaries	n.a.
1a	w940	EBSD	1000 · 500	86.5	95.6	0.50	8 misors	2	0.25	euoz-th25-itjitji-x-1y-1	1.2
1b	w1092	EBSD	1100 · 1400	76.0	89.8	0.50	8 misors	2	0.25	eoz-th50mjtji	2.5
1b	w1092-s30	EBSD	483 · 904	77.3	92.9	0.50	8 misors	2	0.25	eoz-th50mjitji	2.5
2a	w1086	EBSD	1200 · 400	72.0	81.0	0.50	8 misors	2	0.25	eoz-th25-er5-mmmjitji	1.2
2b	w946	EBSD	1500 · 970	94.3	98.6	0.50	8 misors	2	0.25	eoz-th50itji	2.5
3a	w1010-s34	EBSD	450 · 980	82.1	91.2	1.00	8 misors	2	0.50	eoz-th50i-tjitji	2.5
3a	w1010-s36	EBSD	500 · 830	78.5	90.0	1.00	8 misors	2	0.50	eoz-th50i-tjitji	2.5
3b	w935	EBSD	1277 ·1027	92.3	95.6	0.9988	8 misors	2	0.4994	eoz-th32i-e5dH-mjitji	1.5
3b	w965-s40	EBSD	840 · 700	76.9	88.6	1.00	8 misors	4	0.25	ueuoz-th50er5-ttjitji	2.5
3b	w965-s45	EBSD	720 · 1600	89.0	94.8	0.25	8 misors	1	0.25	eoz+m-th40-e5dG-mjitji	2.0

Solid Earth Discuss., doi:10.5194/se-2017-30, 2017
Manuscript under review for journal Solid Earth
Discussion started: 20 March 2017

Solid Earth Discussions
Open Access
EGU

Table 4
Grain size measurements

1	2	3	4	5	6	7	8
Map	Number of grains	Mode v(D)	Standard deviation	μ + σ	μ + 2σ	μ + 3σ	RMS(d)
undeformed Black Hills Quartzite							
BHQ undef. EBSD	216	104.1200	5.3856	109.51	114.89	120.28	77.214
BHQ undef. CIP	1146	103.9600	13.847	117.81	131.65	145.50	89.964
(a) all maps							
1a-w940	5914	5.2979	1.9958	7.2937	9.2895	11.29	4.1186
1b-w1092	34115	4.0942	1.4439	5.5381	6.9820	8.43	3.4025
1b-w1092-s30	9871	4.0790	1.4839	5.5629	7.0467	8.53	3.3308
2a-w1086	4377	5.7705	2.1522	7.9227	10.075	12.23	4.9579
2b-w946	19279	6.5284	2.9552	9.4836	12.439	15.39	4.5242
3a-w1010-s34	6441	9.0813	3.4139	12.495	15.909	19.32	7.9589
3a-w1010-s36	5792	9.2756	3.4170	12.693	16.110	19.53	8.3934
3b-w935	13354	14.5430	6.5298	21.073	27.603	34.13	9.3815
3b-w965-s40	10910	10.9640	4.3534	15.317	19.671	24.02	7.5841
3b-w965-s45	1860	10.0500	4.3044	14.354	18.659	22.96	6.6653
(b) dependence on grain kernel average misorientation (gKAM)							
1b-w1092 high gKAM	19391	3.9213	1.3561	5.2774	6.6335	7.99	3.2697
1b-w1092 low gKAM	14725	4.2960	1.5167	5.8127	7.3295	8.85	3.5699
2b-w946 high gKAM	13406	5.6628	2.4508	8.1136	10.564	13.02	4.0418
2b-w946 low gKAM	6396	7.7984	3.1009	10.899	14.000	17.10	5.4014
3b-w935 high gKAM	7898	13.0990	5.8398	18.939	24.779	30.62	8.6666
3b-w935 low gKAM	6220	16.2140	7.1071	23.321	30.428	37.54	10.267
(c) texture dependence							
1b-w1092 all (center strip)	25553	4.2660	1.4415	5.7075	7.1490	8.59	3.4041
1b-w1092 B-domain	11647	4.6881	1.8084	6.4965	8.3048	10.11	3.4741
1b-w1092 Y-domain	2289	4.1495	1.2075	5.3570	6.5646	7.77	3.2928
2b-w946 all	19280	6.5776	2.9357	9.5133	12.449	15.38	4.5241
2b-w946 B-domain	7425	7.2038	3.3556	10.559	13.915	17.27	4.7579
2b-w946 Y-domain	5634	6.5537	2.8060	9.3597	12.166	14.97	4.4397
3b-w965 all	10910	11.0140	4.3210	15.335	19.656	23.98	7.5828
3b-w965 B-domain	2203	11.5460	4.8128	16.359	21.172	25.98	7.8153
3b-w965 Y-domain	7385	11.0500	4.2983	15.348	19.647	23.94	7.6113
3b-w935 all	13359	14.6840	6.8181	21.502	28.320	35.14	9.3800
3b-w935 B-domain	2817	14.1530	6.8712	21.024	27.895	34.77	9.1574
3b-w935 Y-domain	7702	15.972	7.0684	22.413	29.482	36.55	9.5594

Solid Earth Discuss., doi:10.5194/se-2017-30, 2017
Manuscript under review for journal Solid Earth
Discussion started: 20 March 2017

Solid Earth
Discussions
Open Access
EGU

Figure 1
General shearing experiments on BHQ

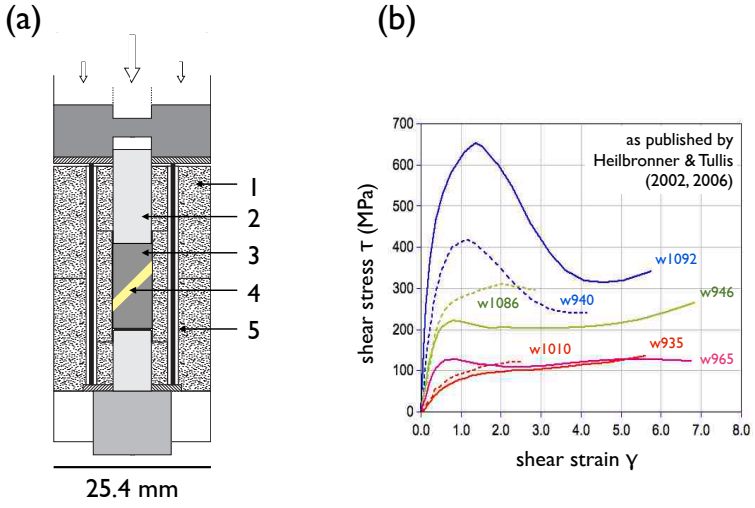

Solid Earth Discuss., doi:10.5194/se-2017-30, 2017
Manuscript under review for journal Solid Earth
Discussion started: 20 March 2017

Solid Earth Discussions
Open Access
EGU

Figure 2
Orientation images

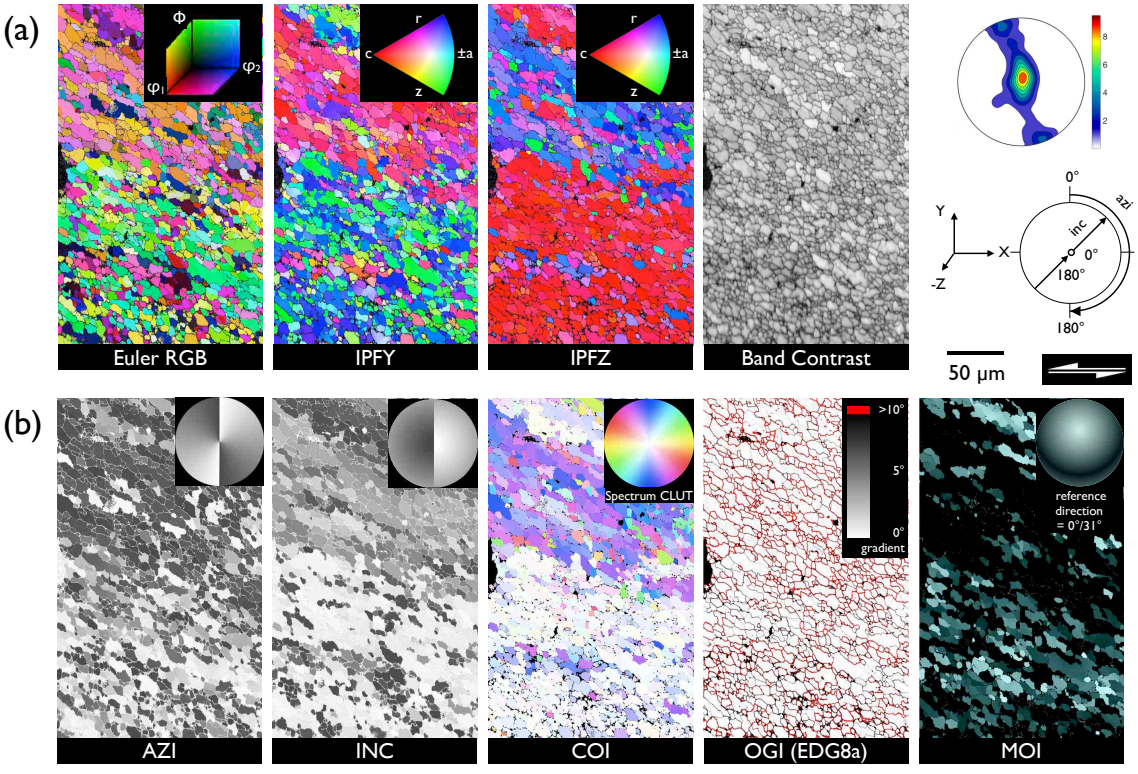

Solid Earth Discuss., doi:10.5194/se-2017-30, 2017
Manuscript under review for journal Solid Earth
Discussion started: 20 March 2017

Figure 3
Segmentation based on texture

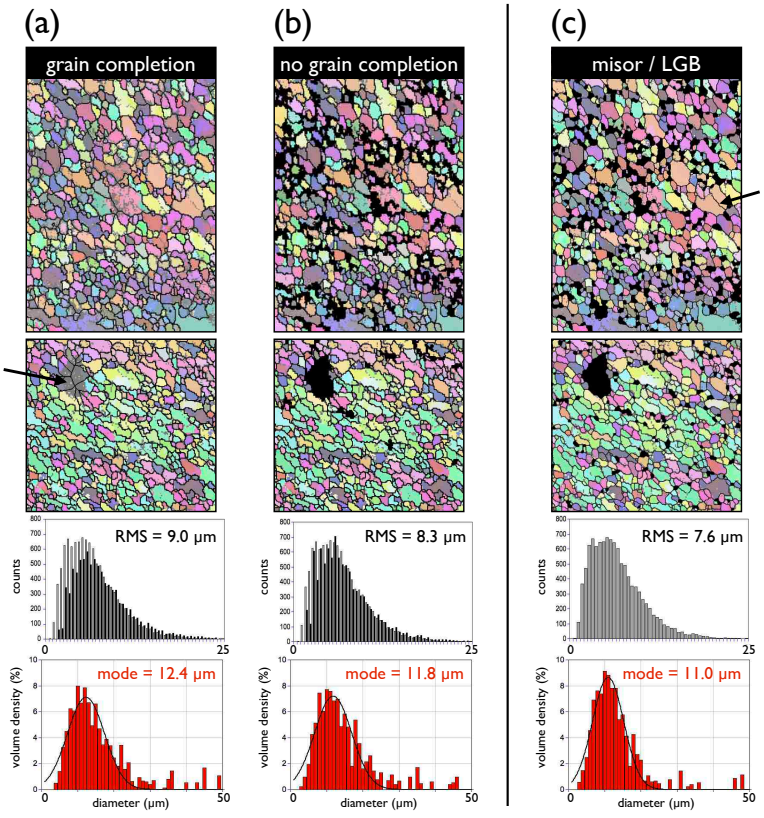

Solid Earth Discuss., doi:10.5194/se-2017-30, 2017
Manuscript under review for journal Solid Earth
Discussion started: 20 March 2017

Figure 4
Grain size maps

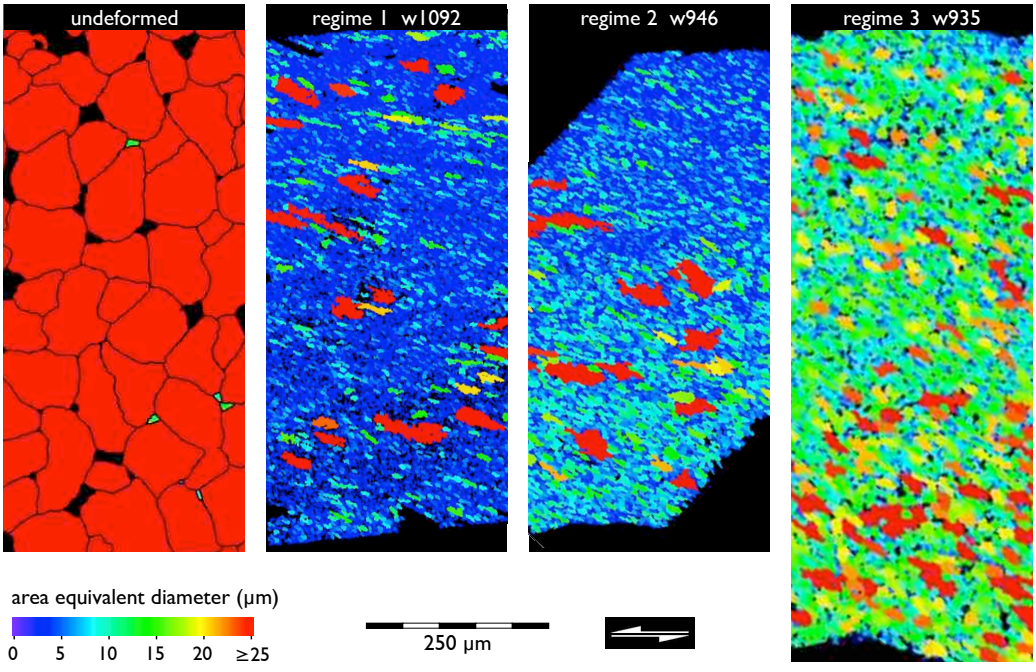

Solid Earth Discuss., doi:10.5194/se-2017-30, 2017
Manuscript under review for journal Solid Earth
Discussion started: 20 March 2017

Figure 5
Recrystallized grain size for regime 1, 2, and 3

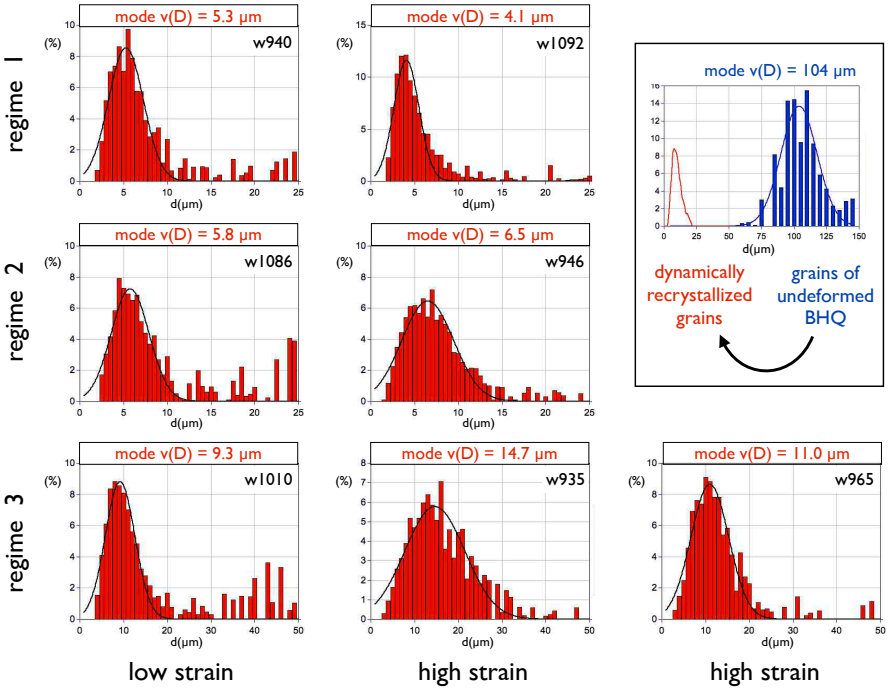

Solid Earth Discuss., doi:10.5194/se-2017-30, 2017
Manuscript under review for journal Solid Earth
Discussion started: 20 March 2017

Figure 6
Details of c-axis texture

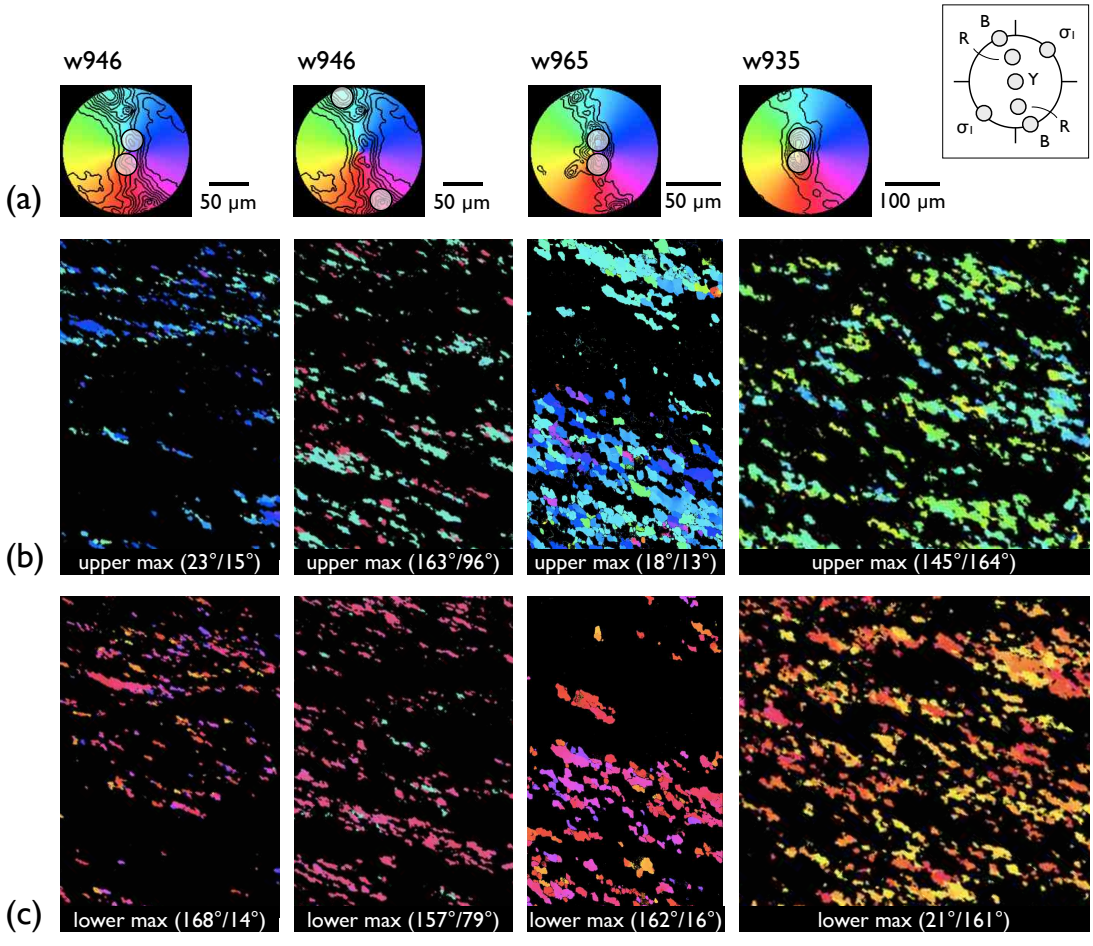

Solid Earth Discuss., doi:10.5194/se-2017-30, 2017
Manuscript under review for journal Solid Earth
Discussion started: 20 March 2017

Figure 7
Recrystallized grain size as f(misorientation density)

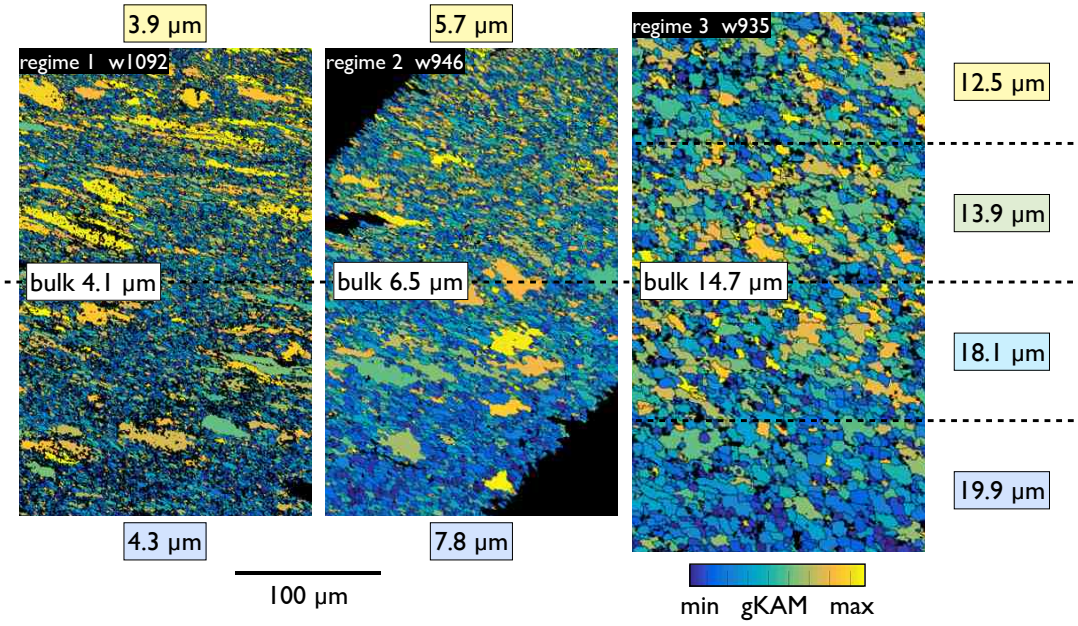

Solid Earth Discuss., doi:10.5194/se-2017-30, 2017
Manuscript under review for journal Solid Earth
Discussion started: 20 March 2017

Figure 8
Mapping grain size in texture domain

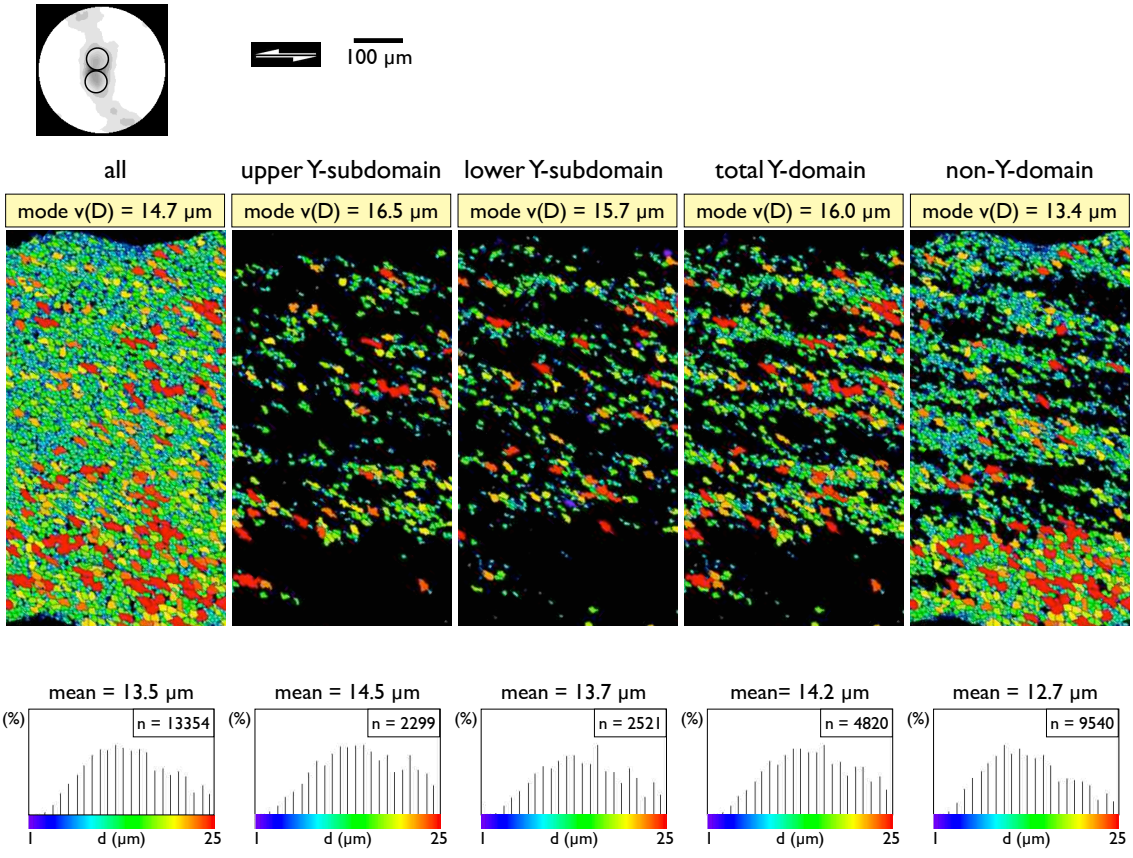

Solid Earth Discuss., doi:10.5194/se-2017-30, 2017
Manuscript under review for journal Solid Earth
Discussion started: 20 March 2017

Solid Earth Discussions
Open Access
EGU

Figure 9
Recrystallized grain size as f(texture)

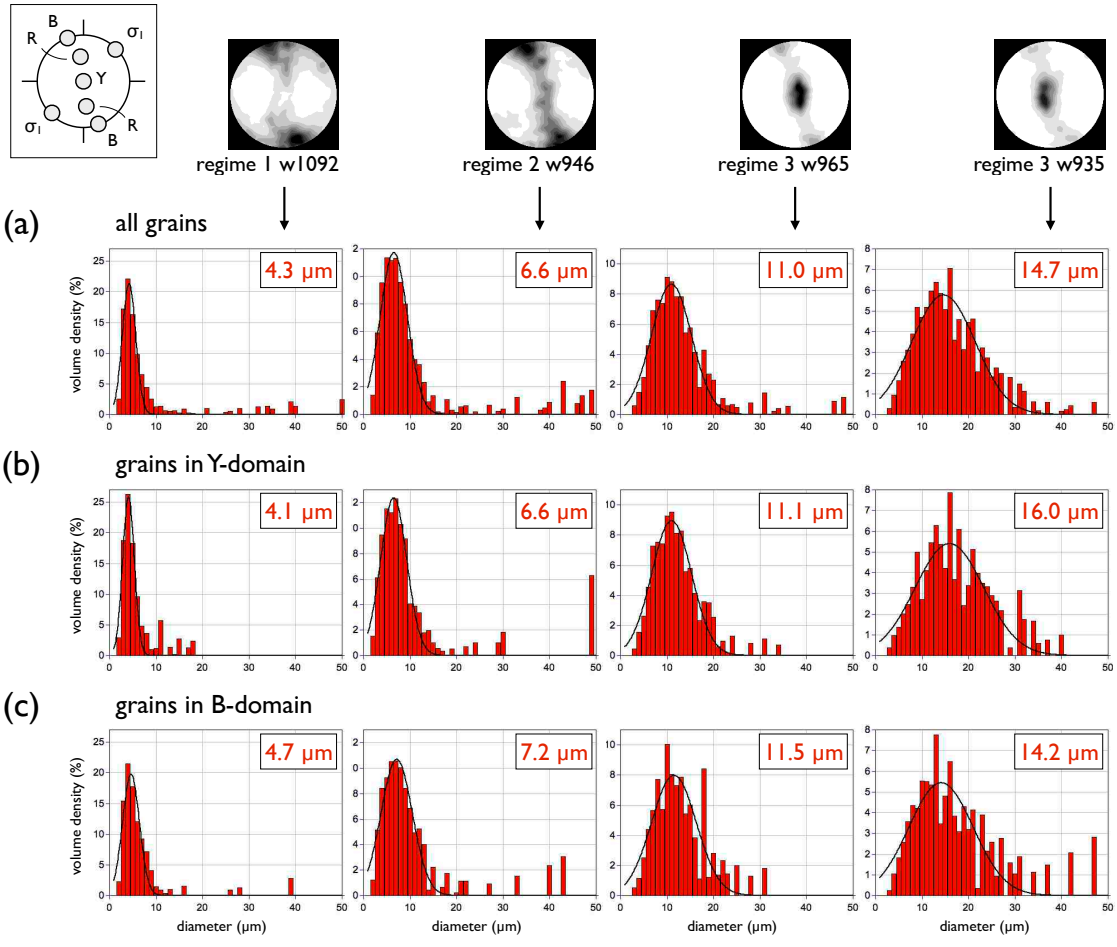

Solid Earth Discuss., doi:10.5194/se-2017-30, 2017
Manuscript under review for journal Solid Earth
Discussion started: 20 March 2017

Figure 10
Recrystallized grain size as f(flow stress)

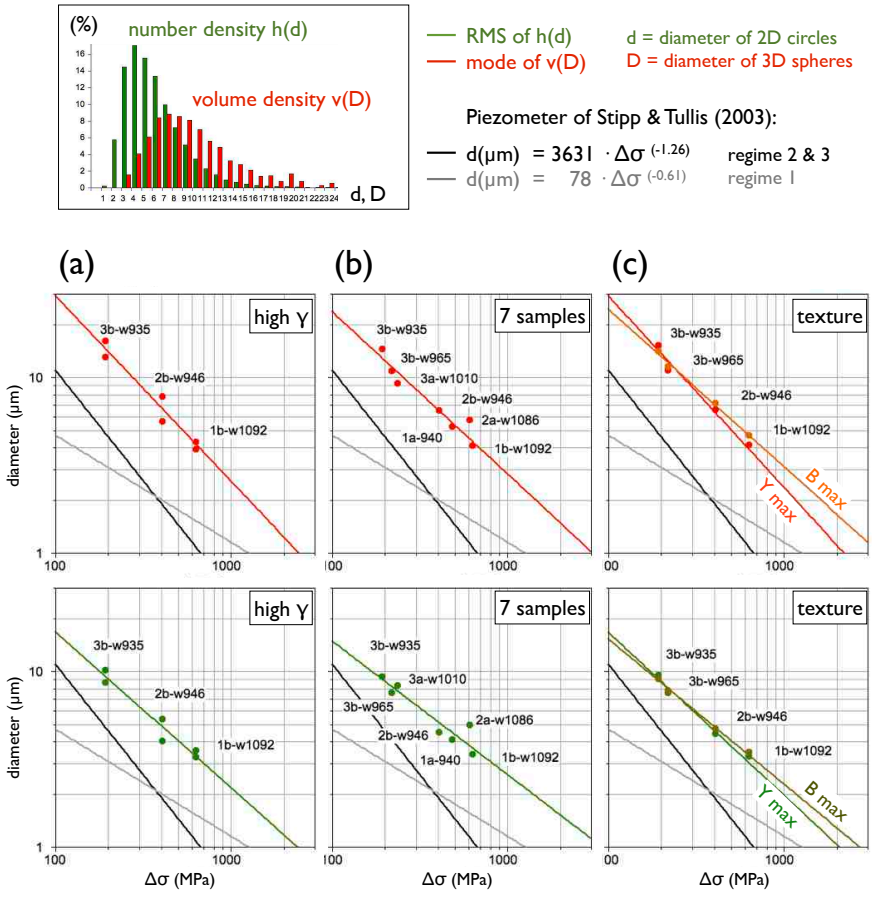

Solid Earth Discuss., doi:10.5194/se-2017-30, 2017
Manuscript under review for journal Solid Earth
Discussion started: 20 March 2017

Solid Earth
Discussions
Open Access
EGU

Figure 11
Comparison CIP versus EBSD

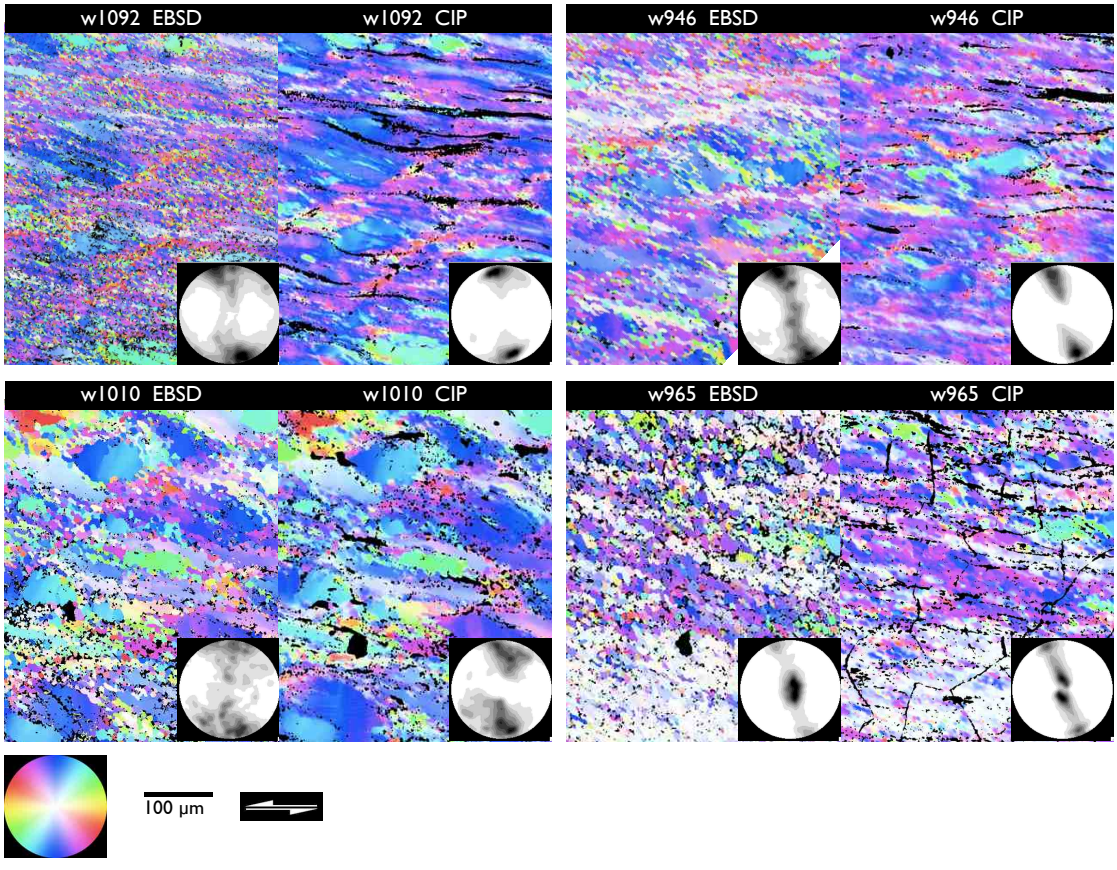

Solid Earth Discuss., doi:10.5194/se-2017-30, 2017
Manuscript under review for journal Solid Earth
Discussion started: 20 March 2017

Solid Earth Discussions
Open Access
EGU

Figure 12
Spatial distribution and cluster size in Y-domain

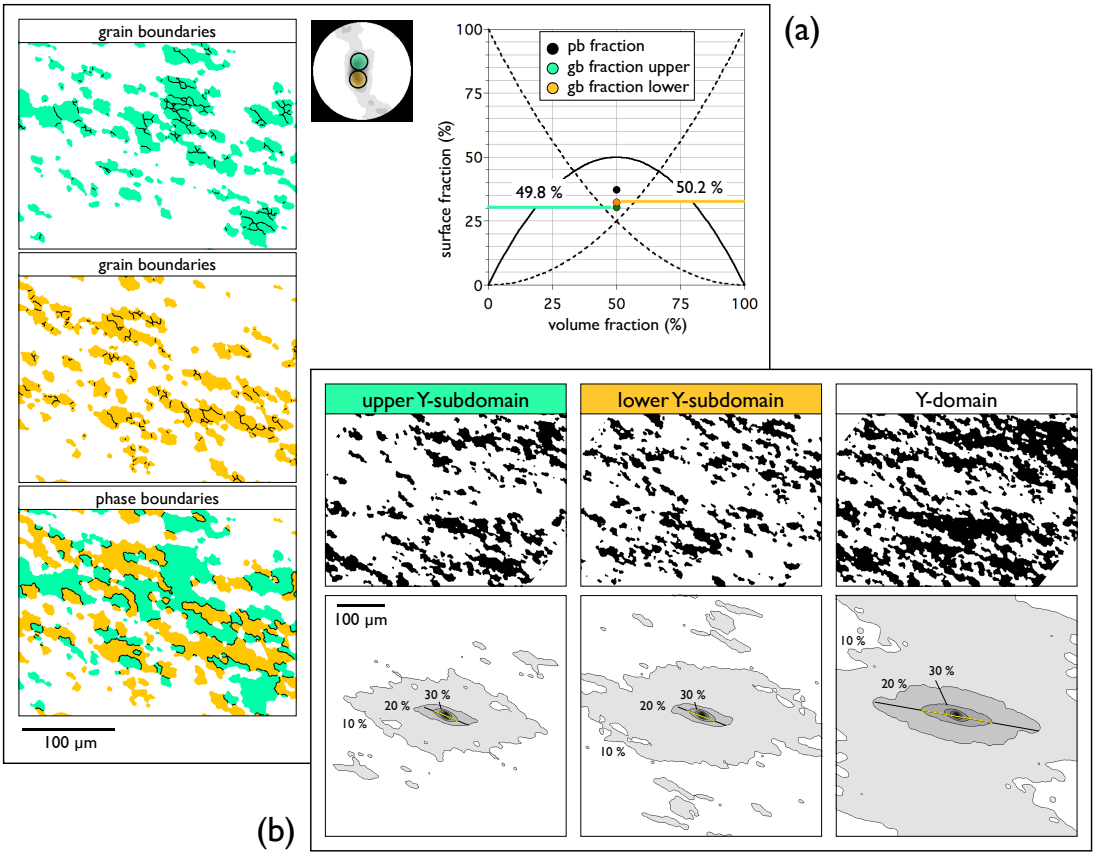

Solid Earth Discuss., doi:10.5194/se-2017-30, 2017
Manuscript under review for journal Solid Earth
Discussion started: 20 March 2017

Solid Earth Discussions
Open Access
EGU

Figure 13
Comparison of segmentations

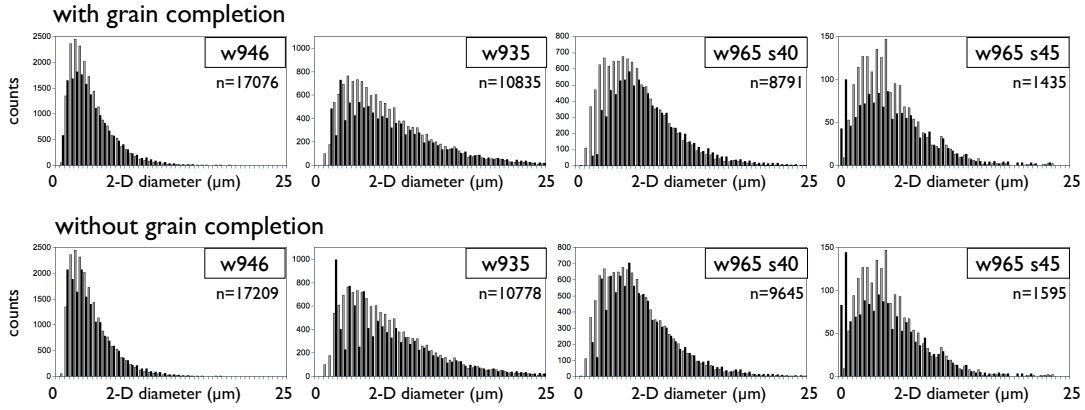

sample	indexing rate (%)	RMS(d) EBSDc	RMS(d) EBSDnc	RMS CIP	RMS ratio CIP/EBSDc (%)	mode v(D) EBSDc	mode v(D) EBSDnc	mode CIP	mode ratio CIP/EBSDc (%)
w946	94.3	4.9373	4.8918	4.5242	91.6	7.4788	7.3889	6.5284	87.3
w935	92.3	10.747	10.509	9.3815	87.3	17.058	16.532	14.543	85.3
w965-s40	76.9	8.9981	8.3442	7.5841	84.3	12.363	11.845	10.964	88.7
w965-s45	89.0	7.4375	6.9302	6.6653	89.6	11.374	10.925	10.05	88.4

Solid Earth Discuss., doi:10.5194/se-2017-30, 2017
Manuscript under review for journal Solid Earth
Discussion started: 20 March 2017

Solid Earth Discussions
Open Access
EGU

Figure 14
Relation of quartz domains and bulk sample strain.